JOURNAL OF GEOPHYSICAL RESEARCH, VOL. 105, NO. C7, PAGES 16,971–16,998, JULY 15, 2000

Alongshore currents over variable beach topography

Donald N. Slinn,[1] J. S. Allen and R. A. Holman

College of Oceanic and Atmospheric Sciences, Oregon State University, Corvallis

Abstract. The nonlinear dynamics of unstable alongshore currents in the nearshore surf zone over variable barred beach topography are studied using numerical experiments. These experiments extend the recent studies of *Allen et al.* [1996] and *Slinn et al.* [1998], which utilized alongshore uniform beach topographies by including sinusoidal alongshore variation to shore parallel sandbars. The model involves finite difference solutions to the nonlinear shallow water equations for forced, dissipative, initial value problems and employs periodic boundary conditions in the alongshore direction. Effects of dissipation are modeled by linear bottom friction. Forcing for the alongshore currents is provided by gradients in the radiation stress, which are specified using linear theory and the dissipation function for breaking waves formulated by *Thornton and Guza* [1983]. Distinct flows develop depending on the amplitude ϵ and wavelength λ of the topographic variability and the dimensionless parameter Q, the ratio of an advective to a frictional timescale. For Q greater than a critical value Q_C the flows are linearly stable. For $\Delta Q = Q_C - Q > 0$ the flow can be unstable. For small values of ΔQ the effect of increasing ϵ is to stabilize or regularize the flows and to cause the mean flow to approximately follow contours of constant depth. Equilibrated shear waves develop that propagate along the mean current path at phase speeds and wavelengths that are close to predictions for the most unstable mode from linear theory applied to alongshore-averaged conditions. At intermediate values of ΔQ, unsteady vortices form and exhibit nonlinear interactions as they propagate along the mean current path, occasionally merging, pairing, or being shed seaward of the sandbar. Eddies preferentially form in the mean current when approaching alongshore troughs of the sandbar and break free from the mean current when approaching alongshore crests of the sandbar. At the largest values of ΔQ examined the resulting flow fields resemble a turbulent shear flow and are less strongly influenced by the alongshore variability in topography. As the amplitude of the alongshore topographic variability increases, alongshore wavenumber-frequency spectra of the across-shore velocity show a corresponding increase in energy at both higher alongshore wavenumbers and over a broader frequency range with significant energy at wavenumbers of topographic variability and harmonics. Across-shore fluxes of mass and momentum generally increase with increasing topographic amplitude and increasing ΔQ. Time- and space-lagged correlations of the across-shore velocity show that correlation length scales decrease as topographic perturbation amplitudes increase. Terms from the vorticity equation show that the alongshore variation of the radiation stresses and the value of ΔQ are of importance to the flow behavior. Hybrid experiments separating effects of spatially variable forcing and the dynamic influence of topography on time-averaged currents show that the effects are generally comparable with the relative importance of each effect a function of ΔQ. The results show that topographic variability has a significant influence on nearshore circulation.

1. Introduction

Observations in the nearshore surf zone of alongshore variations in alongshore currents have been explained as a response to the beach bathymetry. *Bowen* [1969] and *Keely and Bowen* [1977] showed that this could arise through alongshore variations in gradients of the radiation stress, which describes the transfer of momentum

[1]Now at Department of Ocean Engineering, Florida Atlantic University, Boca Raton.

Paper number 2000JC900051.
0148-0227/00/2000JC900051$09.00

from the shoaling wave field to the mean currents. Recent observations at Duck, North Carolina, by *Oltman-Shay et al.* [1989] have found propagating disturbances in alongshore currents that have been interpreted as shear instabilities of the mean currents by *Bowen and Holman* [1989] using linear analysis. Numerical models have shown that these disturbances can become nonlinear and contribute to time dependence in the alongshore currents [*Allen et al.*, 1996]. Another factor in producing alongshore variability in alongshore currents has been suggested by *Putrevu et al.* [1995] and A. J. Reniers et al. (Effects of alongshore nonuniformities on longshore currents measured in the field, submitted to *Journal of Geophysical Research*, 1998), who point to possible contributions from alongshore pressure gradients coupled to the bathymetry. *Wu et al.* [1985] have included contributions from time-averaged nonlinear convective accelerations in their examination of field measurements of alongshore currents over variable topography.

Several fundamental aspects of the dynamical behavior of alongshore currents over nonuniform topography have yet to be explained. How does the resulting flow depend on beach topography, dissipation processes, and the forcing conditions? How do flow instabilities interact with alongshore topographic variations for unsteady flows? Do offshore directed rip currents increase in the presence of rip channels in offshore bars? How do wavelike vorticity disturbances propagate over variable topography? The purpose of our present study is to extend the work of *Allen et al.* [1996] and *Slinn et al.* [1998] to include alongshore variability in the beach topography. The primary objective is to examine the effects that alongshore variations of barred beach topography have on the resulting nonlinear flows.

The numerical experiments of *Allen et al.* [1996] and *Slinn et al.* [1998] involve finite difference solutions to the nonlinear shallow water equations for dissipative, initial value problems with idealized forcing. *Allen et al.* [1996] showed that the flow response over a plane beach depends on a dimensionless parameter $Q = \mu L/V_M h_0$, representing the ratio of an advective to a frictional timescale, where μ is the bottom friction coefficient, V_M is the maximum alongshore velocity, and h_0/L is the beach slope. Below a critical value Q_C the flows are linearly unstable, and disturbances grow initially at the wavelength of the most unstable linear mode. For small values of $\Delta Q = Q_C - Q$ (≥ 0) the waves equilibrate with constant or time-varying amplitudes. For larger values of ΔQ, the unstable waves evolve into longer-wavelength, nonlinear, propagating, steady or unsteady, wavelike disturbances.

The experiments of *Slinn et al.* [1998] include uniform shore parallel sandbars with the radiation stress gradients calculated using the dissipation model of *Thornton and Guza* [1983]. For small values of ΔQ over barred beaches, equilibrated shear waves develop that propagate alongshore at phase speeds and wavelengths that are in agreement with predictions from linear theory for the most unstable linear mode. At intermediate values of ΔQ, unsteady vortices form and interact in a nonlinear manner as they propagate alongshore. At higher values of ΔQ the alongshore current generates vortices that are shed seaward of the bar, creating an energetic eddy field in the region just offshore of the surf zone. The shear waves and eddies diffuse alongshore momentum across shore and may produce strong alongshore currents in the trough where active surface wave breaking is diminished.

Several questions concerning the behavior of alongshore currents in the presence of alongshore variability in topography remain unanswered. Do alongshore variations in the topography stabilize or destabilize the flow? Will disturbances at topographic length scales dominate those at wavelengths of the linearly unstable shear waves? What role do alongshore pressure gradients play in the time-averaged momentum balance for nonlinear flows? How sensitive are the flows to the level of approximation used in formulating the radiation stress model? Are across-shore fluxes of momentum by finite amplitude flow instabilities enhanced by alongshore variability? Do time-averaged currents accelerate when the water depth decreases? How do eddy fields and turbulence respond to alongshore bathymetric variations? We attempt to address these questions by conducting numerical experiments.

Our approach is to select a barred beach profile similar to topography measured at Duck, North Carolina, and perturb it with sinusoidal alongshore variations with wavelength λ and amplitude ϵ. The topography is held fixed for experiments in which the bottom friction coefficient is varied. In the present study we use a two-dimensional radiation stress model coupled to the topography to assess the effects on the time-averaged flow of horizontal momentum diffusion from current instabilities, of pressure gradients, and of variations in the radiation stress gradients. We purposefully avoid complications from the inclusion of additional uncertain horizontal diffusive processes. In these experiments we focus on a study of the dependence of the general characteristics of the flow on the magnitude of Q, ϵ, and λ and do not pursue detailed comparisons with field data. The nature of the flow response is found to depend sensitively on these parameters. Given this sensitivity and the fact that quantitative representations of bottom frictional processes in the surf zone are not well established, we feel the present process-oriented studies are a desirable prerequisite to studies that attempt direct simulations of conditions during field experiments.

The paper is organized into four sections. Section 2 contains the problem formulation. Section 3 describes numerical experiments, and Section 4 gives a summary and conclusions.

2. Formulation

Numerical experiments involving finite difference solutions to the shallow water equations for idealized, forced, dissipative, initial value problems are utilized to study the nonlinear dynamics associated with shear instabilities of alongshore currents in the surf zone over shore parallel sandbars with sinusoidal alongshore variations in the sandbar height. We select the simplest fluid dynamical system that retains the essential physics of this problem. The model geometry is periodic in the alongshore direction and bounded offshore of the region of interest by a vertical wall. Forcing effects from obliquely incident breaking surface waves are approximated by a steady force in the momentum equations. Dissipation is modeled by linear bottom friction. Weak biharmonic friction is included to provide additional numerical dissipation at high wavenumbers in the finite difference solutions. The rigid lid approximation is also invoked.

The governing shallow water equations are employed in dimensional form as

$$(hu)_x + (hv)_y = 0 \,, \tag{1a}$$

$$u_t + uu_x + vu_y = -\frac{p_x}{\rho_0} - \mu\frac{u}{h} + \tilde{F}^{(x)} - \nu\nabla^4 u \,, \tag{1b}$$

$$v_t + uv_x + vv_y = -\frac{p_y}{\rho_0} - \mu\frac{v}{h} + \tilde{F}^{(y)} - \nu\nabla^4 v \,, \tag{1c}$$

where Cartesian coordinates (x, y) are aligned across-shore and alongshore, respectively, where $x = 0$ at the coast, t is time, (u, v) are velocity components in the (x, y) directions, p is pressure, ρ_0 is the constant fluid density, $h = h(x, y)$ is the depth, μ is a bottom friction coefficient, and ν is a small biharmonic diffusion coefficient [*Phillips*, 1959; *Slinn et al.*, 1998; *Durran*, 1999]. Steady forcing terms $\tilde{F}^{(x)}$ and $\tilde{F}^{(y)}$, determined from the gradients of the radiation stress tensor, are applied to the momentum equations to represent momentum input from breaking surface waves.

The rigid lid approximation is utilized [e.g., *Bowen and Holman*, 1989] on the basis of the assumption that the characteristic timescale is the advective timescale $t_C = L_S/V_M$ and on the basis of the scaling estimate that $V_M^2 \ll gh_0$, where g is the acceleration of gravity and V_M is the maximum current velocity over the sandbar in water depth h_0 at $x = x_0 = L_S$. The latter condition is reasonably well satisfied for typical scale values $V_M \approx 1$ m s^{-1} and $h_0 \approx 2$ m. Equivalent wave setup, determined by converting the pressure field induced by the radiation stresses to an equivalent free surface perturbation height η with $g\eta_x = p_x/\rho_0 = \tilde{F}^{(x)}$, for the beach and wave field parameters used below does not greatly change the water depth from the rigid lid values. For example, these conditions would result in setup over the sandbar of $\sim$0.003 m in a mean local water depth of 1.8 m. Near the shoreline, at the pressure grid point closest to the shore ($x_0 = 1$ m) the setup reaches a maximum value of 0.02 m in a depth of water of 0.075 m. For the specified beach slope, including the setup in the water depth would result in moving the shoreline only 0.25 m shoreward, a negligible distance for the processes of our focus. Dynamic effects of wave setup are included directly in the pressure and forcing formulation within the rigid lid approximation.

Allen et al. [1996] showed that $Q = \mu L_S/(V_M h_0)$ is the primary dimensionless parameter upon which the solutions depend. Note that Q represents the ratio of an advective timescale L_S/V_M to a frictional timescale h_0/μ. The numerical experiments reported here are performed in dimensional variables. The dynamical similarity for a specified beach bathymetry and the dependence on the dimensionless parameter Q can be recovered, of course, by rescaling. We adjust Q through variation of μ, where $\mu = C_f|u_{\rm rms}|$. Here $u_{\rm rms}$ is the mean wave orbital velocity, and C_f is the dimensionless bottom friction coefficient. For the primary set of experiments presented below we choose $C_f = 0.02$, 0.015, 0.01, and 0.005, which correspond to values of $\mu = 0.00546$, 0.00409, 0.00273, and 0.00136 m s^{-1} for $|u_{\rm rms}| = 0.273$ m s^{-1}.

The bathymetry of the model is described in Appendix A and shown in Figure 1 for different amplitudes ϵ of alongshore variation. The (x, y) dimensions of the domain are $(L^{(x)}, L^{(y)})$. The model is periodic in the y direction with period $L^{(y)} = 768$ m. We choose $L^{(x)}$ (= 512 m) large enough that the behavior of the flow is not influenced by the finite domain size in x. The sandbar in Figure 1 is centered at $x_C = 80$ m.

The numerical model is described in detail by *Allen et al.* [1996]. It is a finite difference model written in conservation form on a staggered (C) grid using Adams-Bashforth time stepping and a direct Poisson solver to obtain the pressure field. The modification of the pressure solution procedure here for variable topography is described in Appendix B. The grid spacing is uniform ($\Delta x = \Delta y = 2$ m), and the time step $\Delta t \leq 0.2$ s. The biharmonic friction coefficient $\nu = 1.25$ m^4 s^{-1} is set so that the biharmonic friction, which adds numerical damping at small length scales ($\simeq 4$ m), has negligible influence on the dynamics of the instabilities of interest here [*Slinn et al.*, 1998].

The boundary conditions in x correspond to no normal flow at the shore and at the offshore boundary, i.e.,

$$hu = 0, \quad x = 0, L^{(x)} \,. \tag{2}$$

The biharmonic diffusion operator requires the additional boundary conditions

$$u_{xx} = v_x = v_{xxx} = 0, \quad x = 0, L^{(x)} \,. \tag{3}$$

For analysis of the experiments, defining the following variables and averaging operations is useful. The vertical component of vorticity is

$$\zeta = v_x - u_y \,, \tag{4}$$

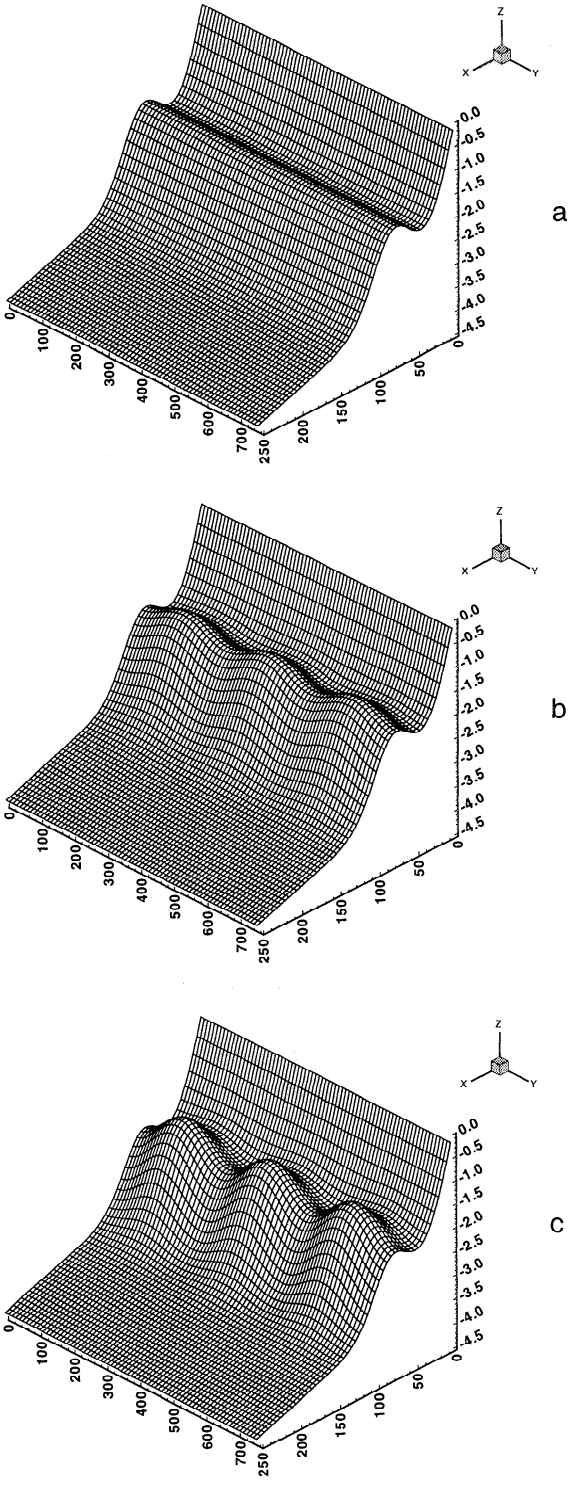

Figure 1. Beach bathymetry for a barred beach with alongshore variations for (a) $\epsilon = 0$, (b) 0.1, and (c) 0.2 and $\lambda = 256$ m.

and the potential vorticity is $q = \zeta/h$. From (1a) a transport stream function may be defined such that

$$hu = -\psi_y \,, \quad hv = \psi_x \,. \tag{5}$$

The alongshore and time averages of a quantity are given by

$$\overline{v} = \frac{1}{L^{(y)}} \int_0^{L^{(y)}} v(x,y,t)\, \mathrm{d}y \,, \tag{6}$$

$$\langle v \rangle = \frac{1}{\Delta t} \int_{t_i}^{t_f} v(x,y,t)\, \mathrm{d}t \,, \tag{7}$$

where $\Delta t = t_f - t_i$. Variables, such as the alongshore velocity, may be divided into mean (time-averaged, alongshore-averaged, or time- and alongshore-averaged) and fluctuating parts, as defined by

$$v(x,y,t) = \langle v \rangle + v'(x,y,t) \,, \tag{8}$$

$$v(x,y,t) = \overline{v} + \tilde{v}(x,y,t) \,, \tag{9}$$

$$v(x,y,t) = \langle \overline{v} \rangle + \hat{v}(x,y,t) \,. \tag{10}$$

Using (8), the time-averaged y momentum equation (1c) can be written as

$$\langle NL \rangle + h \langle p_y \rangle / \rho_0 + \mu \langle v \rangle + h\nu\nabla^4 \langle v \rangle - h\tilde{F}^{(y)} = 0 \,, \tag{11}$$

where $\langle NL \rangle = \langle (huv)_x \rangle + \langle (hvv)_y \rangle$ is the time-averaged nonlinear term. The vorticity equation, formed by cross differentiating the momentum equations and subtracting (1b) from (1c), is

$$\zeta_t + (u\zeta)_x + (v\zeta)_y + \mu\left[\left(\frac{v}{h}\right)_x - \left(\frac{u}{h}\right)_y\right] = \tilde{F}_x^{(y)} - \tilde{F}_y^{(x)} - \nu\nabla^4\zeta \,. \tag{12}$$

The time-averaged vorticity equation is

$$(\langle u \rangle \langle \zeta \rangle)_x + (\langle v \rangle \langle \zeta \rangle)_y + \langle (u'\zeta')_x \rangle + \langle (v'\zeta')_x \rangle + \mu[(\langle v \rangle / h)_x - (\langle u \rangle / h)_y] = \tilde{F}_x^{(y)} - \tilde{F}_y^{(x)} - \nu\nabla^4 \langle \zeta \rangle \,, \tag{13}$$

where the nonlinear terms have been separated into mean components,

$$\overline{NL} = (\langle u \rangle \langle \zeta \rangle)_x + (\langle v \rangle \langle \zeta \rangle)_y, \tag{14}$$

and eddy components

$$NL' = \langle (u'\zeta')_x \rangle + \langle (v'\zeta')_x \rangle \,. \tag{15}$$

We note that with the stream function defined in (5), the vorticity equation (13) provides a single governing equation in one variable ψ. Consequently, the relevant dynamical balances may be determined by an examination of the relative size of the terms in (13).

The radiation stress forcing model (described in Appendix C) utilizes the *Thornton and Guza* [1983] parameterization for the wave energy dissipation by breaking waves and provides steady forcing terms $\tilde{F}^{(x)}$ and $\tilde{F}^{(y)}$ for the momentum equations ((1b) and (1c)). The model parameters are specified in Appendix C.

Depth contours, surface wave ray paths, and $F^{(x)}$ and $F^{(y)}$ (Appendix C) for $\epsilon = 0.2$ are shown in the nearshore region for $0 < y < 512$ m in Plate 1. The rays in Plate 1b indicate regions of convergence near $y = 150$

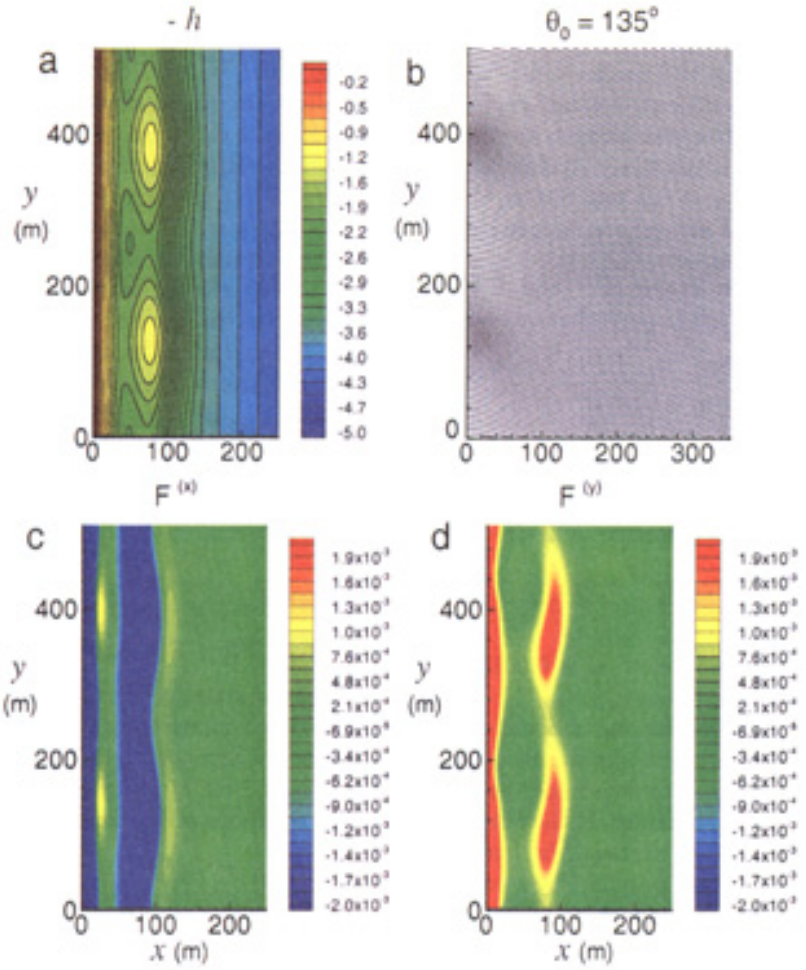

Plate 1. (a) Beach bathymetry h (m), (b) ray paths, and (c) and (d) forcing terms to the momentum equations $F^{(x)}$ and $F^{(y)}$ (m s^{-2}) for $\epsilon = 0.2$ and $\lambda = 256$ m.

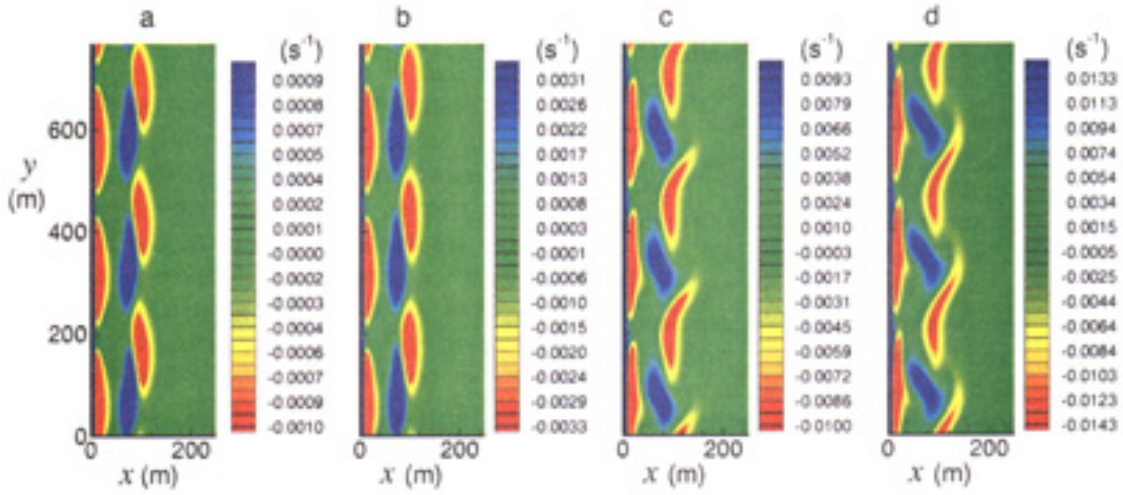

Plate 2. Steady vorticity fields $\zeta(x, y)$ (s^{-1}) for experiments at different values of $\mu > \mu_C$: (a) $\mu = 0.1$, (b)$\mu = 0.03$, (c) $\mu = 0.01$, and (d) $\mu = 0.07$.

and 400 m for $x < 60$ m and regions of divergence near $y = 20$ and $y = 280$ m. $F^{(x)}$ exhibits increased values in the regions of ray convergence and weaker values where the rays diverge. $F^{(y)}$ is also strongly nonuniform in the alongshore direction with strongest alongshore forcing located where the sandbar is relatively shallow at approximately $x = 80$ m and $y = 128$ and 384 m. Note that there is little forcing of alongshore momentum in the trough for $20 < x < 60$ m.

For these experiments the forcing $\tilde{F}^{(x)}$ and $\tilde{F}^{(y)}$ in (1a)–(1c) have small y-dependent perturbations added to $F^{(x)}$ and $F^{(y)}$, i.e.,

$$\tilde{F}^{(x)} = F^{(x)}(x,y)[1 + \alpha b(y)] , \tag{16}$$

$$\tilde{F}^{(y)} = F^{(y)}(x,y)[1 + \alpha b(y)] , \tag{17}$$

where

$$\alpha b(y) = \alpha \sum_{j=1}^{J} b_j \cos\left(2\pi j y / L^{(y)} - \phi_j\right) . \tag{18}$$

For the experiments presented below, $\alpha = 0.001, b_j = 1, J = 12$, and ϕ_j are random phases.

To assess effects of different forcing models, additional experiments were run with forcing specified using different levels of approximation to determine the radiation stresses over variable topography. In the first such approximate system, called the "average $h(x)$ model," $F^{(x)}$ and $F^{(y)}$ are made uniform alongshore by assuming that the topographic variations in y are small and calculating the radiation stresses based upon the alongshore-averaged topography $\overline{h}(x)$. This level of approximation might be invoked as an estimate for weakly varying topography in modeling field data when detailed information about the alongshore variability of the beach bathymetry might be unknown. A second level of approximation to the radiation stress model, called the "local one-dimensional (1-D model)," is described in Appendix C.

Results for steady, linear, frictionally balanced alongshore currents $v(x, y_0)$, at $y_0 = 97$ and 193 m for the wave field parameters specified in Appendix C, for $\mu = 0.1$ m s^{-1}, $\epsilon = 0.2$, and $\lambda = 256$ m, from the two approximate forcing models are compared with the full 2-D model in Figure 2. These results were produced utilizing the finite difference model of (1a)-(1c) and running the experiments until a steady flow developed. Note that the artificially large value of $\mu = 0.1$ m s^{-1} results in small values of $v(x, y)$. At high friction the primary vorticity balance is between gradients of the radiation stress and the bottom stress, with a small contribution from the biharmonic friction for $x < 20$ m, i.e.,

$$\mu\left[(v/h)_x - (u/h)_y\right] + \nu\nabla^4\zeta = \tilde{F}_x^{(y)} - \tilde{F}_y^{(x)} . \tag{19}$$

Note that the corresponding primary momentum balance involves terms representing these same effects plus the pressure gradient terms and can produce regions of negative velocity in recirculation zones for the linear regime. At $y_0 = 97$ m the across-shore position of the alongshore current maxima over the sandbar predicted by the models varies by 15 m. The average $h(x)$ model results in weaker negative currents in the trough and weaker positive currents near the shore than the other models. At $y_0 = 193$ m the magnitudes of the currents over the bar vary by ~50% between the models, with the local 1-D model resulting in substantially stronger currents over the bar and near the shore than the full 2-D model and with the average $h(x)$ model giving the largest deviations from the full 2-D model results. We conclude that the alongshore flows are sensitive to the formulation of the forcing model and recommend, when possible, including the more realistic physics of the 2-D model, which is used throughout the remainder of this study.

3. Results

3.1. Basic Flow Features

The linear stability of the forced velocity profiles over barred beach topography with $\epsilon = 0$ is determined in the standard manner [e.g., *Drazin and Reid*, 1981]. Details are set forth by *Allen et al.* [1996] and *Slinn et al.* [1998]. Solutions of the form

$$\tilde{\psi} = Re\left\{\phi(x)\exp\left[ik(y - (c_r + ic_i)t)\right]\right\} \tag{20}$$

are obtained numerically from the linearized potential vorticity equation as a function of the alongshore wavenumber k. The biharmonic diffusion terms are included as by *Slinn et al.* [1998]. The real part of the phase speed c_r gives the alongshore rate of propagation of the linear modes, while the imaginary part multiplied by k gives the growth rate kc_i. Positive values of kc_i indicate unstable modes, while negative values indicate modes that decay in time.

The growth rate kc_i for the most unstable linear mode is plotted as a function of k in Figure 3 for different values of the bottom friction coefficient μ for experiments with $\epsilon = 0$. The velocity profiles used in the linear stability calculations are the steady linear frictionally balanced alongshore currents that would result from a balance between forcing, friction, and biharmonic friction (i.e., $V_{TGE}(x)$ by *Slinn et al.* [1998]). These are linearly unstable at the specified values of μ, with the fastest growing linear mode having a wavelength of ~134 m. The growth rates increase as μ is decreased. The e-folding times of the fastest growing linear modes are 1.34, 2.86, 5.85, and 17.4 min. For the high friction case, $\mu = 0.00546$ m s^{-1}, unstable modes are predicted for wavelengths between 88 and 228 m, while the low friction case, $\mu = 0.00136$ m s^{-1}, has positive growth rates for wavelengths between 60 and 768 m, where 768 m is the largest wavelength examined in the stability calculation. For $\mu \geq \mu_C = 0.006337$ m s^{-1}

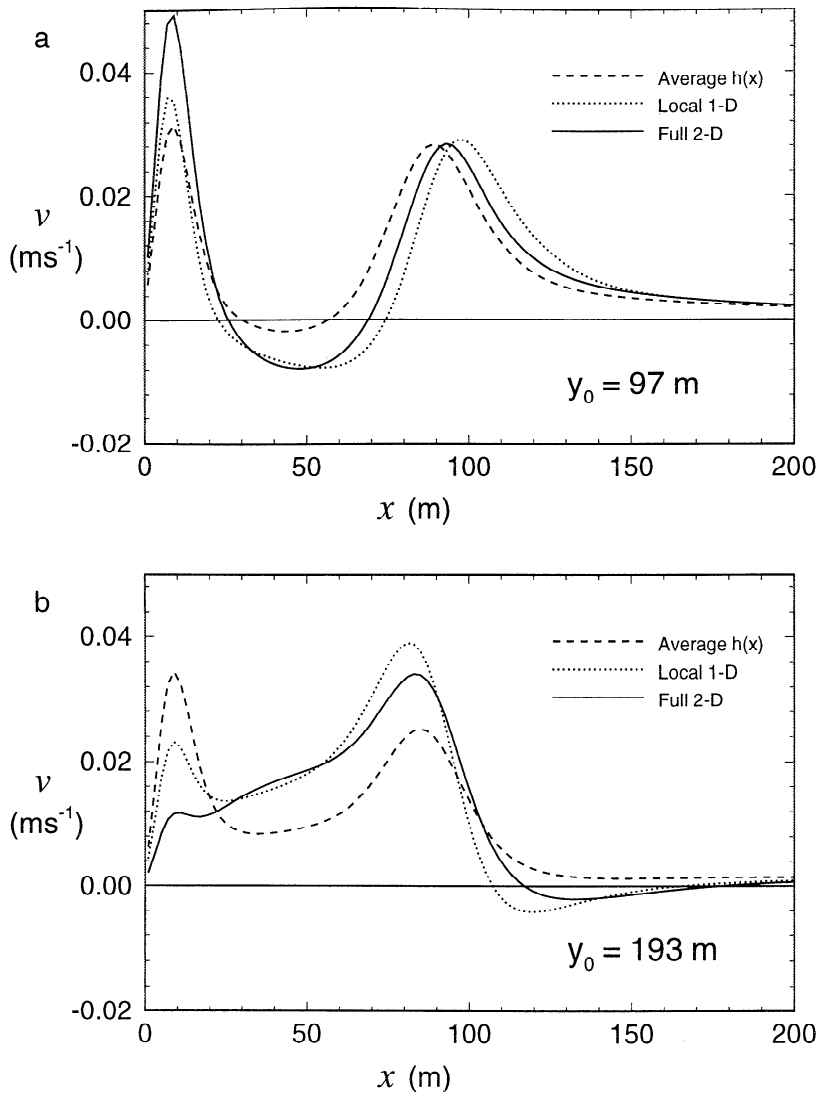

Figure 2. Steady alongshore velocity profiles $v(x, y_0)$ at (a) $y_0 = 97$ and (b) $y_0 = 193$ m that result for $\mu = 0.1$ m s^{-1} for three different radiation stress models: the uniform alongshore approximation, a local one-dimensional approximation, and the full two-dimensional model.

the flow is linearly stable. We denote the corresponding critical value of $Q = 0.738$ as Q_C, such that for $Q \geq Q_C$ the flow is linearly stable for $\epsilon = 0$. The ratio $\Delta Q/Q_C = (Q_C - Q)/Q_C$ gives a measure of how far from the critical stability condition the experiments are conducted. Values of $\Delta Q/Q_C$ for experiments with $\epsilon = 0$ shown in Figure 3 are listed together with other experimental parameters in Table 1.

Linear stability analysis is not applied for flows with $\epsilon > 0$ because the steady alongshore velocity fields are functions of y in addition to x. Growth rates of energy in different alongshore modes at early (linear) times for variable alongshore topography are discussed in Appendix D.

Steady vorticity fields from experiments with values of $\mu > \mu_C$ for $\epsilon = 0.2$ are shown in Plate 2. Note that the contour levels of vorticity are different in Plates 2a–2d, generally varying as μ^{-1}. For $\mu > 0.1$ m s^{-1} the flows are approximated by the linear balance between friction and forcing (19). For decreasing μ, nonlinear effects become increasingly important, and the vorticity is advected alongshore from localized sources generally following contours of constant depth.

The numerical experiments are started with the fluid at rest and run for 10 hours. Time series of the cross-shore velocity u at the location $(x_0, y_0) = (79, 3)$ m for $\epsilon = 0$ and $\epsilon = 0.2$ are shown in Figure 4. For $\mu = 0.00546$ m s^{-1} and $\epsilon = 0$ fluctuations develop into a regular pattern of oscillations with an amplitude of about 0.09 m s^{-1} with a time mean of zero after approximately $t = 2$ hours. The regularity of the fluctuations corresponds, as will be shown, to periodic wavelike be-

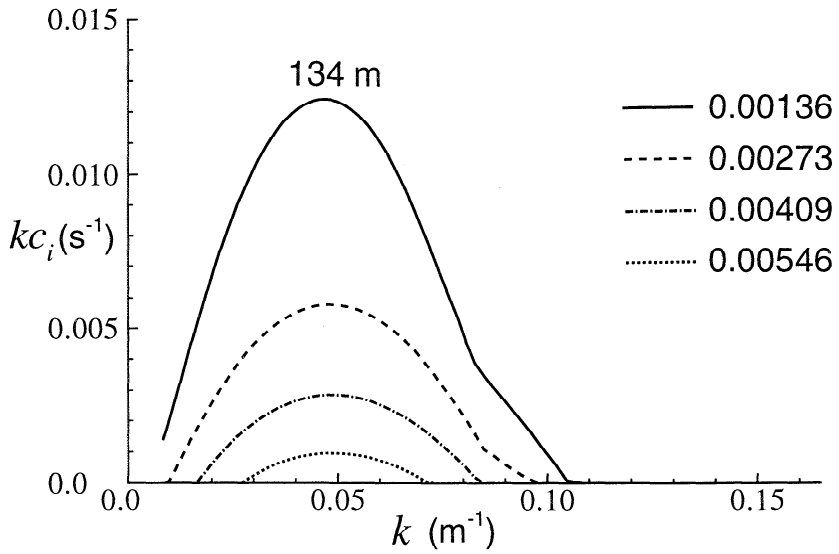

Figure 3. Results of the linear stability calculations for frictionally balanced alongshore velocity profiles in terms of growth rate kc_i versus alongshore wavenumber k for experiments with $\epsilon = 0$ at different values of μ (m s^{-1}). The value of the approximate wavelength $\lambda_M = 2\pi/k$ m at the maximum growth rate is indicated.

havior. As the bottom friction coefficient μ is decreased, for $\epsilon = 0$, the amplitudes and frequencies of the oscillations in the u time series increase, and the fluctuations become more irregular.

For $\mu = 0.00546$ m s^{-1} and $\epsilon = 0.2$ the flow achieves a steady state by $t = 1$ hour with $u = 0.15$ m s^{-1} at this location. Thus at high friction, close to μ_C, an effect of alongshore topographic variability is to stabilize the flow. At $\mu = 0.00409$ m s^{-1} and $\epsilon = 0.2$ the time series of across-shore velocity shows regular fluctuations similar to the wavelike pattern for $\mu = 0.00546$ m s^{-1} and $\epsilon = 0$ but with a time mean of $\sim$0.1 m s^{-1}. In this regime of moderate friction at $\mu = 0.00409$ m s^{-1} the effect of topographic variability is again to make the flow

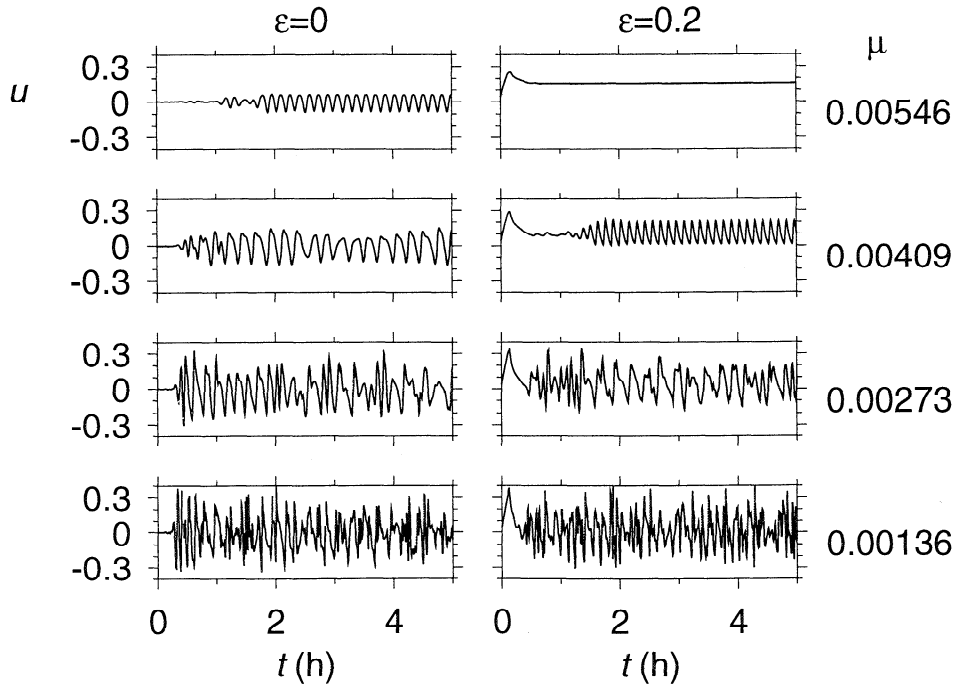

Figure 4. Time series of across-shore velocity component $u(x_0, y_0, t)$ (m s^{-1}) at $x_0 = 80$ m, $y_0 = 0$ from experiments with (a) $\epsilon = 0$ and (b) $\epsilon = 0.2$ with different values of μ from top to bottom $\mu = 0.00546$, 0.00409, 0.00273, and 0.00136 (m s^{-1}).

Table 1. Parameters From Experiments

ϵ	μ, m s^{-1}	λ, m	Q	$\frac{\Delta Q}{Q_C}$	V_{TGEm}, m s^{-1}	M, m^3 s^{-1}
0	0.00546	∞	0.550	0.258	0.463	
0	0.00409	∞	0.312	0.579	0.613	
0	0.00273	∞	0.141	0.810	0.907	
0	0.00136	∞	0.036	0.951	1.759	
0.1	0.00546	256 m				
0.1	0.00409	256 m				
0.1	0.00273	256 m				
0.1	0.00136	256 m				
0.2	0.00546	256 m				
0.2	0.00409	256 m				
0.2	0.00273	256 m				
0.2	0.00205	256 m				
0.2	0.00136	256 m				
0.1	0.00273	768 m				2.178
0.1	0.00273	384 m				1.176
0.1	0.00273	256 m				0.697
0.1	0.00273	128 m				0.370
0.1	0.00273	77 m				0.430

The amplitude of the alongshore topographic perturbation ϵ, the bottom friction coefficient μ, the wavelength of the topography λ, the governing dimensionless parameter Q, the instability parameter $\Delta Q/Q_C = (Q_C - Q)/Q_C$, the local maximum of the forcing profile V_{TGEm} over the sandbar, and the average across-shore meanders of time-averaged stream functions M defined in (21).

less unstable. As friction decreases further at $\epsilon = 0.2$, the stabilizing effect of the topographic variability becomes less apparent from the time series as the fluctuations become increasingly irregular. The time mean of u is positive at this location for $\epsilon = 0.2$, while it is negligibly small for $\epsilon = 0$, as expected from continuity for a homogeneous flow.

Note from Figure 4 that the observable growth of the disturbances occurs at later times for the higher frictional cases, as expected from the results of the linear stability analysis. Since the time of development of the instabilities depends on the magnitude of the perturbations present, we do not attach particular significance to the initial flow behavior.

Instantaneous vorticity fields from experiments at four frictions and $\epsilon = 0$, 0.1, and 0.2 are shown at $t = 10$ hours in Plate 3. At fixed values of ϵ, decreasing the friction leads to more complex vorticity fields. For $\epsilon = 0$ the flow progresses through the different flow regimes described by *Slinn et al.* [1998] as equilibrated shear waves ($\mu = 0.00546$ m s^{-1}), fluctuating eddies confined to the current ($\mu = 0.00409$ m s^{-1}), stronger eddies that break away from the alongshore jet ($\mu = 0.00273$ m s^{-1}), and a turbulent shear flow in which the energetic eddy field in the alongshore current fills the near-shore region and continuously sheds eddies that populate a region offshore of the sandbar ($\mu = 0.00136$ m s^{-1}).

For $\mu = 0.00546$ m s^{-1} and $\epsilon = 0$ the shear waves have an alongshore wavelength of 128 m, agreeing with the length scale predicted for the fastest growing unstable linear mode in Figure 3. For $\epsilon = 0.1$ and 0.2, however, the vorticity fields at $\mu = 0.00546$ m s^{-1} are steady, and the 256 m wavelength alongshore fluctuations in the vorticity fields do not propagate alongshore as do the equilibrated shear waves for $\epsilon = 0$. In these cases the steady currents meander alongshore approximately following contours of constant depth.

At $\mu = 0.00409$ m s^{-1} and $\epsilon = 0.2$ an equilibrated flow response develops in which a shear wave (dominant wavelength 128 m) propagates along the curvilinear path of the time mean current. The shear wave also contains energy at harmonics in wavenumber and frequency (Figure 5) that propagate at twice the phase velocity of the dominant wave. The combination of these modes results in a pulsating pattern of vorticity disturbances (seen in flow visualizations) with the second faster wave traveling through the first wave. For $\mu = 0.00409$ m s^{-1} and $\epsilon = 0.1$ the shear wave fluctuates with weak irregularity as it propagates. At $\mu = 0.00409$ m s^{-1} and $\epsilon = 0$ the fluctuations are stronger, and the dominant alongshore wave length for the vorticity waves increases to ~190 m.

At the lower frictional values $\mu = 0.00273$ and 0.00136 m s^{-1} the vorticity fields are strongly nonlinear, and eddy dynamics play a significant role so that at fixed friction the vorticity fields have a similar appearance independent of the amplitude of the topographic perturbation. For experiments at the lowest friction, $\mu = 0.00136$ m s^{-1}, the region outside of the sandbar from $x = 100$–400 m contains an energetic eddy field created by eddies shed from the alongshore currents in an unsteady manner.

3.2. Statistical Description

The differences between the steady flows, the equilibrated shear waves, and the progressively more unsteady cases at lower friction are illustrated by the alongshore wavenumber-frequency spectra of the across-shore velocities in Figure 5 for different values of ϵ and μ with $\lambda = 256$ m. The spectra in these experiments are calculated from $u(x_0, y, t)$ at $x_0 = 100$ m. This value of x_0 is generally close to the location of the maximum of $\langle v \rangle$. (The characteristics of $\langle v \rangle$ are discussed later and shown in Figure 6.) For the highest frictional case, $\mu = 0.00546$ m s^{-1} and $\epsilon = 0$, the energy is strongly localized at the particular point $(k, \omega) = (0.0491\ \mathrm{m}^{-1}, 0.0109\ \mathrm{s}^{-1})$. Approximately 2 orders of magnitude more energy are found at this (k, ω) point than at any other point. The corresponding wavelength is $\lambda_e = 2\pi/k = 128$ m, and the period is $T_w = 2\pi/\omega = 576$ s. This wavelength agrees with the estimate from the vorticity field in Plate 3, which shows six disturbances with alongshore length scales of 128 m, and this period agrees with that observed from the u time series in Figure 4. Note additionally that

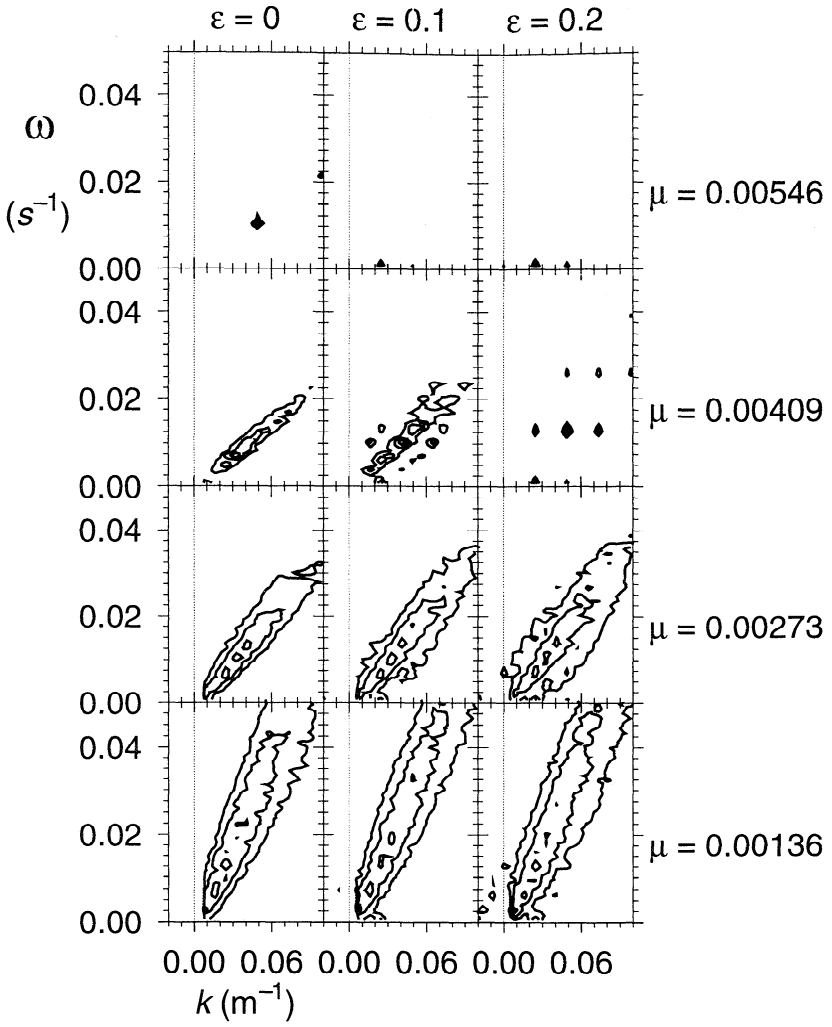

Figure 5. Alongshore wavenumber-frequency (k, ω) spectra for the across-shore velocity $u(x_0, y, t)$ from experiments with different values of μ and ϵ for $\lambda = 256$ m. The spectra are calculated utilizing Fourier transforms in y and t for an 8 hour portion of the experiments (from $t = 2$ hours to $t = 10$ hours) at the offshore location $x_0 = 100$ m. The spectra are calculated using a cosine taper on the first and last 10% of the time series, and the resulting spectra are band-averaged over five frequencies. The contour levels are 10^{-1}, 10^{0}, and 10^{1} m^2 s^{-2}.

there is also a local energy maximum at the harmonic $(k, \omega) = (0.098\ \text{m}^{-1}, 0.0218\ \text{s}^{-1})$ corresponding to twice the (k, ω) values of the maximum in energy. For $\epsilon = 0.1$ and 0.2 at $\mu = 0.00546$ m s^{-1} all of the energy is contained at zero frequency, and the flows are steady. The wavenumber of the energy maximum is at $k = 0.0245$ m^{-1} corresponding to the wavelength of the topography $\lambda = 256$ m with additional energy at higher harmonics.

As friction μ is decreased, with $\epsilon = 0$, the spectra show progressive spreading of the energy to higher and lower wavenumbers and frequencies. The energy remains concentrated about a line representing a linear relation between ω and k but progressively fills a wider band about that line for decreasing friction. For the case $\mu = 0.00409$ m s^{-1} the energy is in a fairly narrow band, around the line $\omega = 0.31k$, suggestive of nondispersive waves moving at the phase speed $c_0 = 0.31$ m s^{-1}.

At $\mu = 0.00409$ m s^{-1} and $\epsilon = 0.2$ the energy maximum is located at $(k, \omega) = (0.049\ \text{m}^{-1}, 0.0131\ \text{s}^{-1})$, corresponding to a wave with $\lambda_e = 128$ m and $c_0 = 0.27$ m s^{-1}. In this case the energy is distributed to both higher harmonics in ω and k and to subharmonics in k that include a zero-frequency component at the scale $\lambda = 256$ m of the topography.

The experiment at $\mu = 0.00409$ m s^{-1} and $\epsilon = 0.1$ contains properties of the flow behavior at both $\epsilon = 0$ and $\epsilon = 0.2$. Energy is primarily contained in a band about the dominant phase velocity but also spreads to higher and lower wavenumbers similar to the harmonics that dominate for $\epsilon = 0.2$.

At the lower frictions the energy is spread to higher wavenumbers and to higher frequencies for all of the values of ϵ but is still primarily concentrated about a line representing a linear relation between ω and k. At $\mu = 0.00273$ m s^{-1} the energy is spread to a broader

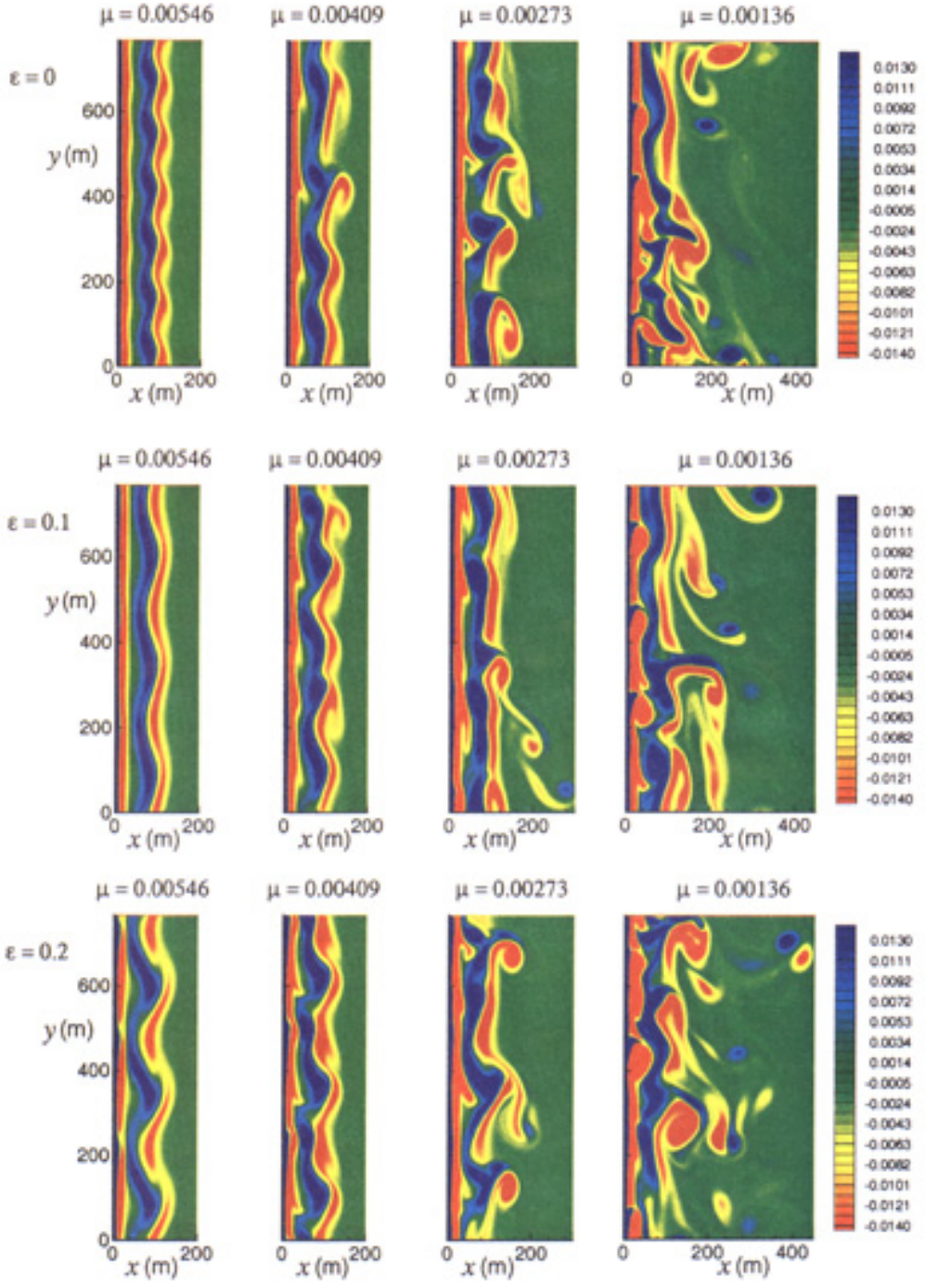

Plate 3. Contour plots of vorticity $\zeta(x, y, t)$ (s^{-1}) fields at $t = 10$ hours for experiments with different values of ϵ and μ (m s^{-1}). The blue contours indicate positive vorticity, the yellow and red regions represent negative vorticity, and the green background regions have near-zero vorticity.

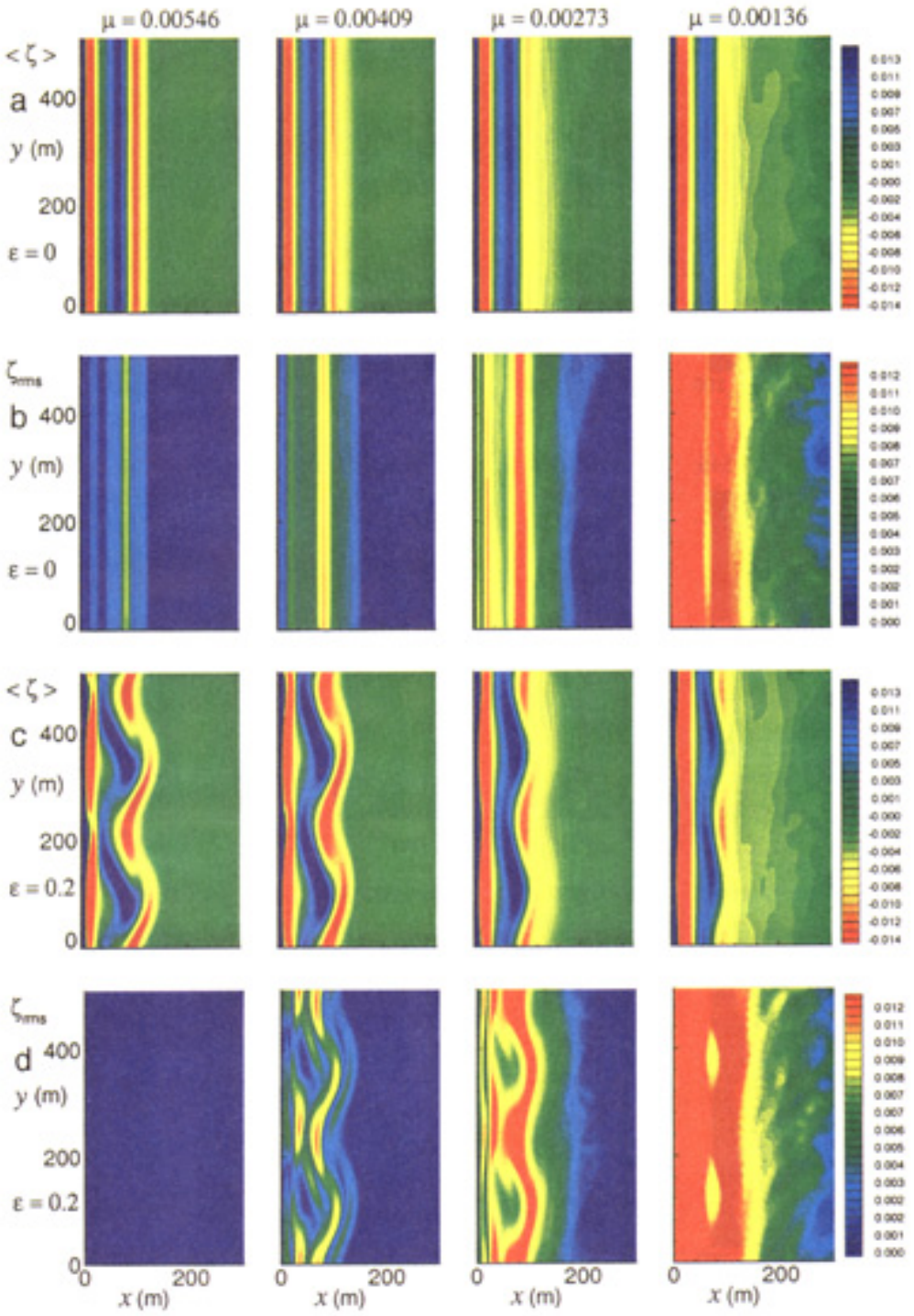

Plate 4. The (a) and (c) time-averaged vorticity $\langle\zeta\rangle\,(x,y)$ (s^{-1}) and the (b) and (d) rms vorticity fluctuations $\langle(\zeta(x,y,t)-\langle\zeta\rangle\,(x,y))^2\rangle^{1/2}$ (s^{-1}) for experiments with $\epsilon = 0$ (Plates 4a and 4b) and $\epsilon = 0.2$ (Plates 4c and 4d) for different values of μ (m s^{-1}). The time averages are for 8.3 hours from $t = 1.7$ hours to $t = 10$ hours.

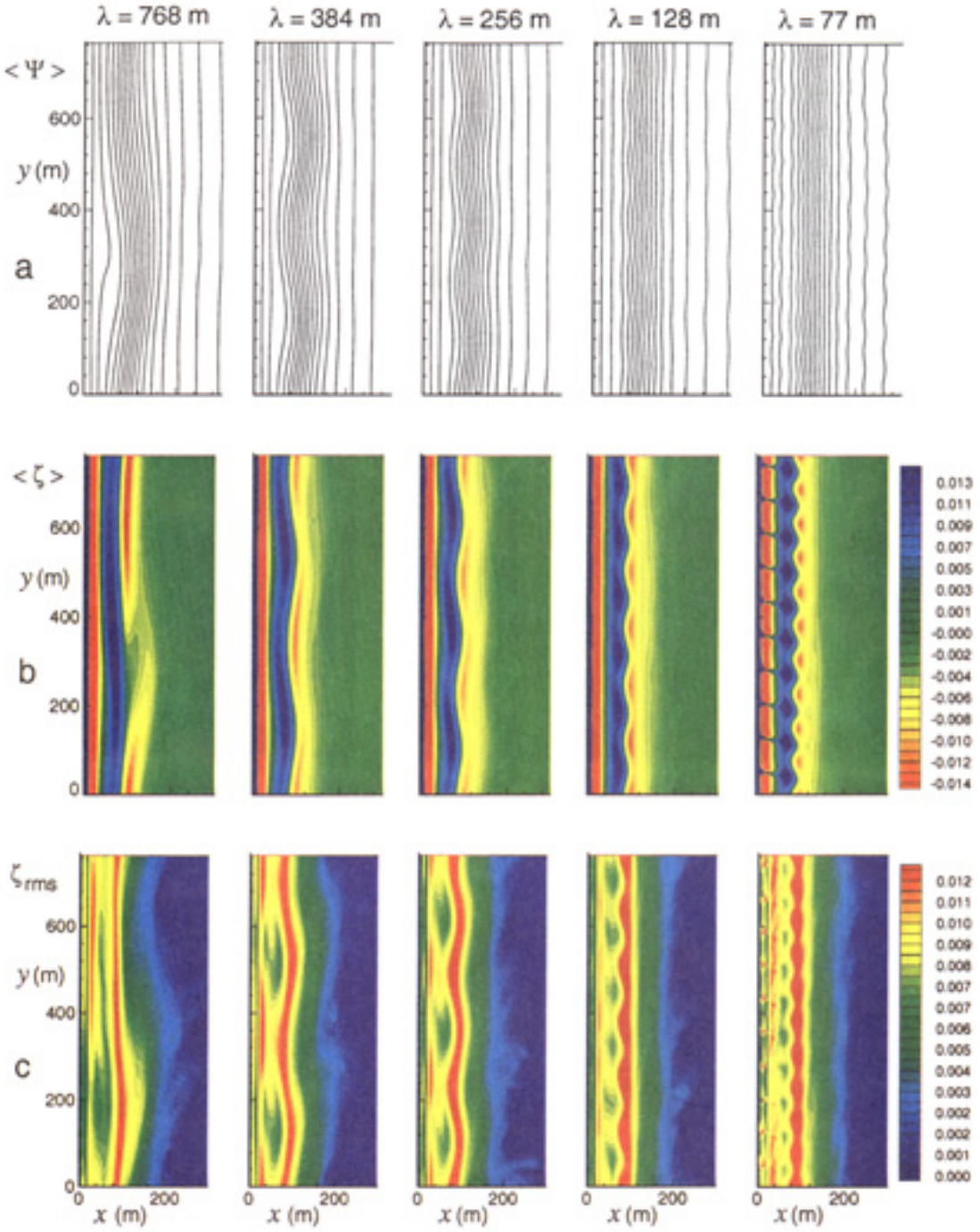

Plate 5. (a) Nondimensional time-averaged stream function $\tilde{\psi} = \langle\psi\rangle/h_0 L_0 V_0$, (b) time-averaged vorticity $\langle\zeta\rangle(x, y)$ (s^{-1}), and (c) rms vorticity fluctuations $\langle(\zeta(x, y, t) - \langle\zeta\rangle(x, y))^2\rangle^{1/2}$ (s^{-1}) for experiments with $\epsilon = 0.1$ and $\mu = 0.00273$ m s^{-1} for different values of topographic wavelength λ. The time averages are for 8.3 hours from $t = 1.7$ hours to $t = 10$ hours. The values of $h_0 L_0 V_0$ from left to right are 85.19, 86.04, 87.69, 91.03, and 89.28 m^3 s^{-1}, where $L_0 = 89$ m, $h_0 = 1.82$ m, and the contour interval for the streamlines is 0.1.

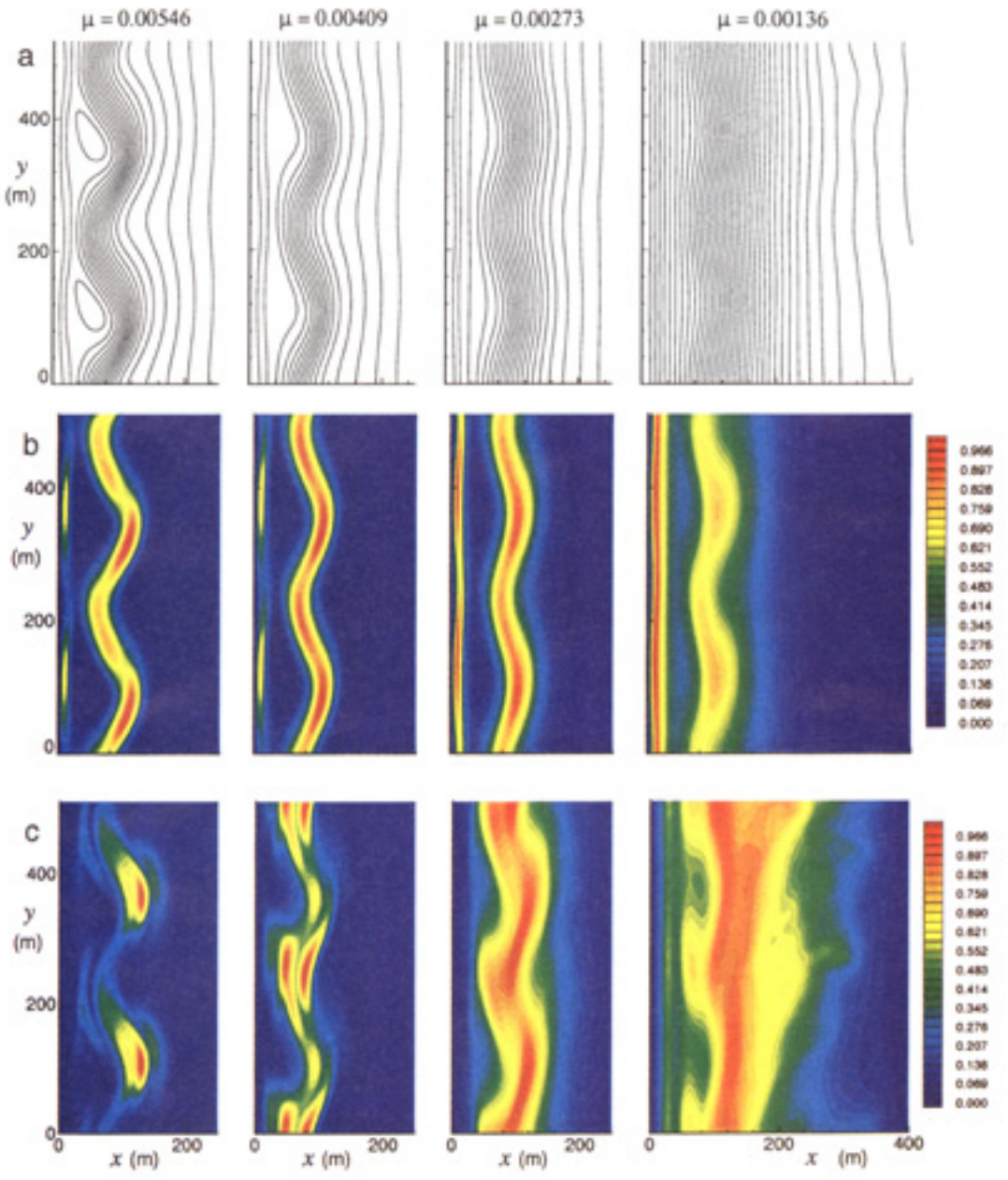

Plate 6. (a) Nondimensional time-averaged stream function $\tilde{\psi} = \langle\psi\rangle/h_0L_0V_0$, (b) normalized mean kinetic energy density $\langle\tilde{\mathrm{KE}}\rangle = 0.5h\langle u^2 + v^2\rangle/\langle\mathrm{KE}_{\mathrm{max}}\rangle$, and (c) normalized time-averaged perturbation kinetic energy density $\langle\tilde{\mathrm{KE}}'\rangle = 0.5h\langle u'^2+v'^2\rangle/\langle\mathrm{KE}'_{\mathrm{max}}\rangle$ for experiments with $\epsilon = 0.2$ with different values of μ (m s^{-1}). The values of $h_0L_0V_0$ are 47.43, 67.85, 87.22, and 123.67 m^3 s^{-1}, where $L_0 = 89$ m, $h_0 = 1.82$ m, and the contour interval for the streamlines is 0.07; $\langle\mathrm{KE}_{\mathrm{max}}\rangle = 0.2022$, 0.2801, 0.3693, and 0.7744 m^3 s^{-2} and $\langle\mathrm{KE}'_{\mathrm{max}}\rangle = 6.16 \times 10^{-8}$, 0.00957, 0.03213, and 0.0751 m^3 s^{-2} for $\mu = 0.00546$, 0.00409, 0.00273, and 0.00136 m s^{-1}, respectively. The time averages are for 8.3 hours from $t = 1.7$ hours to $t = 10$ hours.

range of wavenumbers and to higher frequencies as ϵ increases. At $\mu = 0.00136$ m s^{-1} differences with ϵ are still detectable but are less significant as each flow has similar phase velocity and distribution of energy at high ω and k.

To examine the effect of the choice of x_0 on the estimate of $c_0 = \omega/k$, alongshore wavenumber-frequency spectra from the vorticity fields were calculated for different across-shore positions of $40 < x_0 < 160$ m. The resulting energy distributions and estimates for c_0 are remarkably independent of x_0 and of the local mean velocities $\langle v \rangle$. One difference observed in the spectra at $x_0 = 40$ m, only for experiments at $\mu = 0.00273$ m s^{-1}, is a second band of energy with an apparent phase velocity close to the time-mean alongshore current velocity $\langle v \rangle$ of the inner jet, which is centered at approximately $x_0 = 20$ m. The energy levels in this band are approximately an order of magnitude lower than the energy in the shear wave band at this offshore location. This evidently reflects the fact that although most of the disturbances propagate alongshore as waves, some energy near the shore is carried with the mean currents.

To examine the effect of the alongshore domain length $L^{(y)}$ on the flow, an additional experiment was run with $L^{(y)} = 1536$ m for a bottom friction coefficient of $\mu = 0.00273$ m s^{-1}, $\lambda = 256$ m, and $\epsilon = 0.2$. This experiment produced results essentially equivalent to those obtained with $L^{(y)} = 768$ m. In particular, the resulting (ω, k) spectra for $u(x_0, y, t)$ are nearly identical to those shown in Figure 5. We conclude that the important flow characteristics found in the basic experiments with $L^{(y)} = 768$ m remain unchanged for increased values of $L^{(y)}$.

The time mean vorticity fields $\langle \zeta(x, y) \rangle$ are plotted in Plate 4 for different values of μ for $\epsilon = 0$ (Plate 4a) and $\epsilon = 0.2$ (Plate 4c). The vorticity fields are averaged over an 8.3 hour period, from $t = 1.7$ hours to $t = 10$ hours, and shown in the near-shore region $0 < x < 300$ m, $0 < y < 512$ m. Note the truncation of the domain in y. The rms vorticity fluctuations $\zeta_{\text{rms}} = \langle [\zeta(x, y) - \langle \zeta(x, y) \rangle]^2 \rangle^{1/2}$ about the mean are shown in Plate 4b ($\epsilon = 0$) and Plate 4d ($\epsilon = 0.2$) for the same time period.

For $\epsilon = 0$ the time-averaged vorticity fields illustrate the alongshore uniformity of the flows and the increasing offshore extent of the mean currents for decreasing μ. The rms vorticity fields indicate increasing magnitudes and the across-shore extent of the fluctuations for the lower frictional experiments.

For $\epsilon = 0.2$ the time-averaged vorticity fields clearly indicate the wavelength ($\lambda = 256$ m) of the topography at all frictional values. Except in the steady case $\mu = 0.00546$ m s^{-1}, the topographic variability is also evident in the rms vorticity fluctuations, even for the turbulent shear flow regime at $\mu = 0.00136$ m s^{-1}. As friction decreases, the mean alongshore velocities increase, and the magnitude of the across-shore meander of the time-averaged vorticity fields decreases, evidently reflecting increasing inertial effects. Note that for both $\epsilon = 0$ and 0.2, there are relative minima in the rms vorticity fields located at approximately $x = 75$ m, where the mean vorticity is largest. The mean and rms vorticity fields from the experiments in Plate 4 show three significant effects from topographic variability. First, the mean currents meander alongshore approximately following contours of constant depth; second, the rms vorticity fluctuations also tend to align along contours of constant depth; and third, at higher values of μ, topographic variations tend to stabilize or regularize the flow.

Nondimensional stream functions $\tilde{\psi} = \psi/h_0 L_0 V_0$ from the time mean currents and time mean and rms vorticity fields for $\mu = 0.00273$ m s^{-1} and $\epsilon = 0.1$ for different values of the topographic wavelength between $\lambda = 768$ and 77 m are shown for an 8.3 hour time period in Plate 5. For the constants used in the nondimensionalization, we fix $L_0 = 89$ m as the typical x location of the maximum of $\langle \overline{v} \rangle$, determine $h_0 = \overline{h}(x = L_0) = 1.82$ m, and choose $V_0 = \langle \overline{v} \rangle (x = L_0)$. As a result, $V_0 = 0.526$, 0.531, 0.542, 0.562, and 0.551 m s^{-1} for $\lambda = 768$, 384, 256, 128, and 77 m, respectively. Clear response at the topographic length scale is observed in the mean and rms fields for these nonlinear flows. The strength of the across-shore meanders M of the time-averaged stream functions, defined by

$$M = \frac{1}{L^{(x)}} \int_0^{L^{(x)}} m(x)\, dx\,, \tag{21a}$$

$$m(x) = \left\{ \overline{[\langle \psi(x, y) \rangle - \langle \overline{\psi(x)} \rangle]^2} \right\}^{1/2}, \tag{21b}$$

is given in Table 1 for the experiments shown in Plate 5. A direct comparison of the mean streamlines with the contours of constant depth indicates that for $\lambda \geq 256$ m, the mean streamlines actually have greater across-shore deflections while for $\lambda \leq 128$ m, the opposite is true. In addition to the variations with λ of the spacing between alongshore topographic crests, the experiments differ in a number of ways that can have a dynamic impact on the flows. These differences include the changes in $F^{(x)}$ and $F^{(y)}$ dependent on λ and the changes in the alongshore topographic slope h_y over the sandbar, which decreases as λ increases. Increased across-shore meandering of the mean current occurs for $\lambda \geq 128$ m. For the two experiments with $\lambda \leq 128$ m the mean and rms vorticity fields appear to vary in intensity more dramatically in the alongshore direction but with less change in the across-shore position.

Wavenumber-frequency spectra for the experiments with different values of λ (not shown) at $\mu = 0.00273$ m s^{-1} and $\epsilon = 0.1$ are very similar. As λ decreases, there is a slight increase in energy at higher wavenumbers and frequencies. The largest difference is that

for each experiment, there is a local maximum of energy at the wavenumber of the topography at zero frequency. Other integrated quantities such as $\langle \overline{v} \rangle (x)$ and $\langle \overline{\mathrm{KE}'} \rangle (x)$ are also similar for experiments at different values of λ.

Nondimensional stream functions $\tilde{\psi}$ from the time mean currents, normalized time-mean kinetic energy density $\langle \tilde{\mathrm{KE}} \rangle = 0.5h\langle u^2+v^2 \rangle / \langle \mathrm{KE}_{\max} \rangle$, and normalized time-mean perturbation kinetic energy density $\langle \tilde{\mathrm{KE}}' \rangle = 0.5h\langle u'^2+v'^2 \rangle / \langle \mathrm{KE}'_{\max} \rangle$ are shown for the 8.3 hour time period at different values of μ for $\epsilon = 0.2$ and $\lambda = 256$ m in the region $0 < x < 250$ m ($0 < x < 400$ m for $\mu = 0.00136$ m s^{-1}) and $0 < y < 512$ m in Plate 6. Note again the truncation of the domain in y. The wavelength of the topography is apparent in both the stream functions and the kinetic energy fields as the alongshore current follows a curvilinear path, moving closer to shore in the deeper regions and moving outside of the sandbar's central location ($x = 80$ m) in the shallower regions.

For decreasing μ the mean current follows straighter alongshore paths. Across-shore diffusion of the alongshore momentum increases for decreasing μ as indicated by the broader across-shore extent of closely spaced streamlines, which reflect regions of relatively larger alongshore flow.

For $\mu = 0.00546$ m s^{-1} the flow is steady, and there is a region of flow recirculation in the trough indicated by the closed streamlines located at approximately $x = 60$ m and $y = 120$ and 360 m. The values of $\mathrm{KE}_{\max}$ and $\mathrm{KE}'_{\max}$ are listed in the Plate 6 caption. We note that the $\mathrm{KE}'_{\max}$ is approximately 5 orders of magnitude smaller for $\mu = 0.00546$ m s^{-1} than for experiments at lower friction. For decreasing friction the perturbation energy grows stronger but remains focused about the path of the strongest mean currents. For all of the experiments with $\epsilon = 0.2$ the mean and perturbation kinetic energies exhibit significant alongshore nonuniformity. Stronger mean kinetic energy is observed at alongshore positions close to $y = 128$ and 384 m where the sandbar is largest, the water is shallowest, and the mean current is farthest from the shoreline.

The perturbation (eddy) kinetic energy for the lower frictional experiments, $\mu = 0.00273$ and 0.00136 m s^{-1}, is strongest in regions where the mean current is directed offshore. Comparison of the offshore positions of the mean and perturbation energy for these experiments shows that eddies preferentially break away (offshore) from the mean current at locations where the mean current is directed offshore near the point of its farthest offshore excursion. Weaker eddy energy density within the mean current downstream of these locations supports the conclusion that the eddies preferentially leave the mean current as it meanders offshore around alongshore crests in the sandbar.

Time-averaged velocity profiles $\langle v(x, y_0) \rangle$ at alongshore locations $y_0 = 65$, 129, 193, and 257 m for $\epsilon = 0$ and 0.2 at $\mu = 0.00409$ and 0.00136 m s^{-1} from an 8 hour portion of the experiments ($2 < t < 10$ hours) are shown in Figure 6. For $\epsilon = 0$, there is little variation in the time averages at the different alongshore positions. For $\mu = 0.00409$ m s^{-1} and $\epsilon = 0$ there is relatively weak mean alongshore flow in the trough located near $x_0 = 40$ m of $\langle v \rangle \approx 0.07$ m s^{-1} compared to the current speed over the sandbar at $x_0 = 90$ m of $\langle v \rangle \approx 0.45$ m s^{-1}. For $\mu = 0.00136$ m s^{-1} and $\epsilon = 0$ the mean current speeds in the trough are $\sim$0.60 m s^{-1} compared to peak velocities over the sandbar of $\sim$0.80 m s^{-1} showing the effectiveness of the nonlinear shear instabilities at diffusing alongshore momentum into the trough.

For the experiments with $\epsilon = 0.2$ the results are more complex. For $\mu = 0.00409$ m s^{-1} the location of the maximum of $\langle v \rangle$ over the sandbar varies between approximately $x_0 = 75$ and 100 m at different y_0. This result is consistent with the meandering streamlines in Plate 5, showing that the mean flow approximately follows contours of constant depth. The water depth over the sandbar is maximum at $y_0 = 256$ m, minimum at $y_0 = 128$ m, and at intermediate values at $y_0 = 65$ (upslope) and 193 m (downslope). A first look at Figure 6 might suggest that variations in the alongshore topography for $\mu = 0.00409$ m s^{-1} are effective at producing stronger alongshore currents in the trough. Further consideration reveals, however, that this is a local effect (in regions of deeper water) associated with surface wave breaking and forcing through $F^{(y)}$ occurring nearer to the shore. At other alongshore positions (in regions of shallower water), surface wave breaking occurs farther offshore, and the mean alongshore current forms farther offshore and results in comparatively weaker current velocities in the trough. Thus for $\epsilon = 0.2$, there are weaker alongshore currents in the trough $\langle v \rangle = 0.02$ m s^{-1} than for $\epsilon = 0$ at some alongshore positions (where the trough is shielded by a larger sandbar) and stronger alongshore currents in the trough $\langle v \rangle = 0.20$ m s^{-1} at other alongshore positions (where the sandbar is smaller than for the $\epsilon = 0$ case).

For $\epsilon = 0.2$ and $\mu = 0.00136$ m s^{-1} the location of the alongshore current maximum over the bar does not vary significantly with y_0 as is also shown by the streamlines of Plate 6. The velocity maxima over the sandbar vary from $\sim$0.85 m s^{-1} at the location of shallowest water ($y_0 = 129$ m) to 0.75 m s^{-1} at the location of the deepest water ($y_0 = 257$ m), suggesting that this may be partially related to the conservation of mass; that is hv tends to remain nearly constant. For this experiment the current velocities in the trough are approximately equal at each alongshore location and almost as large as the values over the uniform beach. At low friction the effects of alongshore topographic variability do not increase the strength of the currents in the trough, which result from turbulent eddy fluxes.

Time- and space-lagged correlations

$$C(y_L, t_L) = \frac{\langle\, u'(x_0, y_0 + y_L, t + t_L)\, u'(x_0, y_0, t)\,\rangle}{\langle\, u'^2(x_0, y_0 + y_L, t + t_L)\,\rangle^{1/2}\ \langle\, u'^2(x_0, y_0, t)\,\rangle^{1/2}} \quad (22)$$

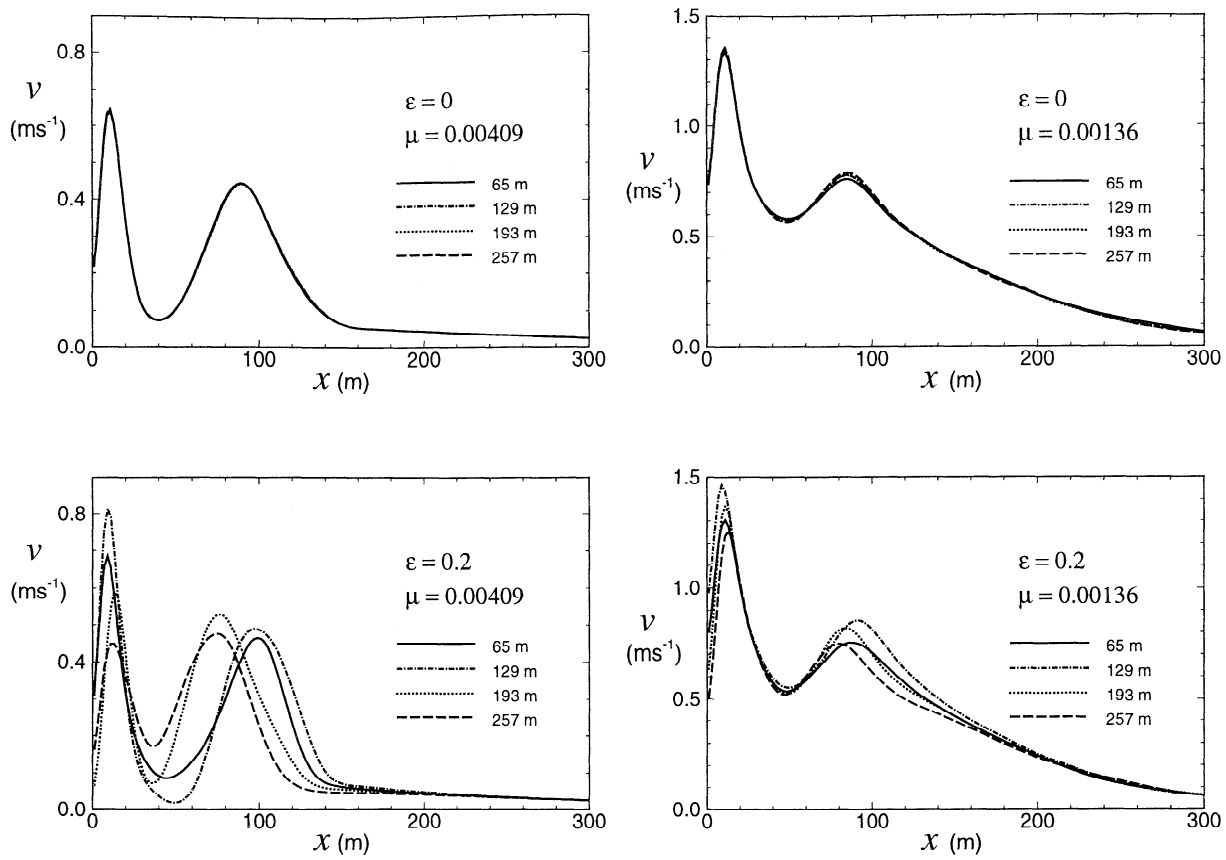

Figure 6. Time-averaged alongshore currents $\langle v \rangle$ at different values of y_0 as a function of x from experiments with $\mu = 0.00409$ and $\mu = 0.00136$ m s^{-1} for both $\epsilon = 0$ and 0.2.

are presented in Figure 7 for $\mu = 0.00273$ m s^{-1} at $c = 0$, 0.1, and 0.2 from time series of $u(x_0, y_0, t)$ at $x_0 = 100$ m and $y_0 = 0$ m. Contour levels between 0.5 and 1.0 are shown. The regions of high correlations indicate the propagating nature of the flow. For $\epsilon = 0$, making estimates from the $C = 0.8$ contour, approximately constant correlations exist along lines with slope $c_0 = y_L/t_L = 0.30$ m s^{-1}, indicating wave propagation at that velocity in close agreement with the estimate obtained previously from the wavenumber-frequency spectra of 0.307 m s^{-1}.

For $\epsilon = 0$, time and space correlation scales determined simply as the lag to 0.5 correlation along $y_L = 0$ and $t_L = 0$ give $t_C \approx 1.4$ min and $y_C \approx 28$ m, respectively. The time and space correlation scales calculated along the line of high correlation $c_0 = y_L/t_L = 0.30$ m s^{-1} are substantially larger. Determined by the lag to correlation of 0.5, these are $t_P \approx 18$ min and $y_P \approx 300$ m.

For $\epsilon = 0.1$ the correlation scales along the line of high correlation are decreased to $t_P \approx 11$ min and $y_P \approx 220$ m. For $\epsilon = 0.2$ the scales are decreased further to $t_P \approx 9$ min and $y_P \approx 170$ m. Qualitatively similar results are obtained at other frictional values, supporting the result that at $\lambda = 256$ m the correlation scales decrease as ϵ increases. Results for different values of λ for fixed $\mu = 0.00273$ m s^{-1} and $\epsilon = 0.1$ did not show significant variation in the correlation length scales.

3.3. Across-Shore Fluxes

The time- and alongshore-averaged across-shore mass flux $\langle \overline{hu} \rangle$ is necessarily zero from continuity. In order to compare integrated across-shore mass fluxes from different experiments we define the quantity $hu_+ = hu$ when $u > 0$ and $hu_+ = 0$ for $u < 0$ and call $\langle \overline{hu}_+ \rangle$ the positive time- and alongshore-averaged across-shore mass flux. The quantity $\langle \overline{hu}_+ \rangle$ is plotted in Figure 8 as a function of x for the 12 experiments with $\lambda = 256$ m. The largest positive across-shore mass fluxes in the region $40 < x < 150$ m are observed for cases with $\epsilon = 0.2$. This region is strongly dominated by the meandering mean flow above the sandbar and the steady case, $\mu = 0.00546$ m s^{-1}, has the highest value. As friction decreases, the mass flux decreases, and the location of the maximum shifts somewhat seaward. For $\epsilon = 0.1$ the mass fluxes decrease by approximately one half, and the same trends with μ occur. For $\epsilon = 0$ the alongshore averages are essentially zero over the sandbar. For all of the experiments with $\mu = 0.00136$ m s^{-1}, there is a significant and approximately equivalent mass flux due to the eddy field between $200 < x < 500$ m.

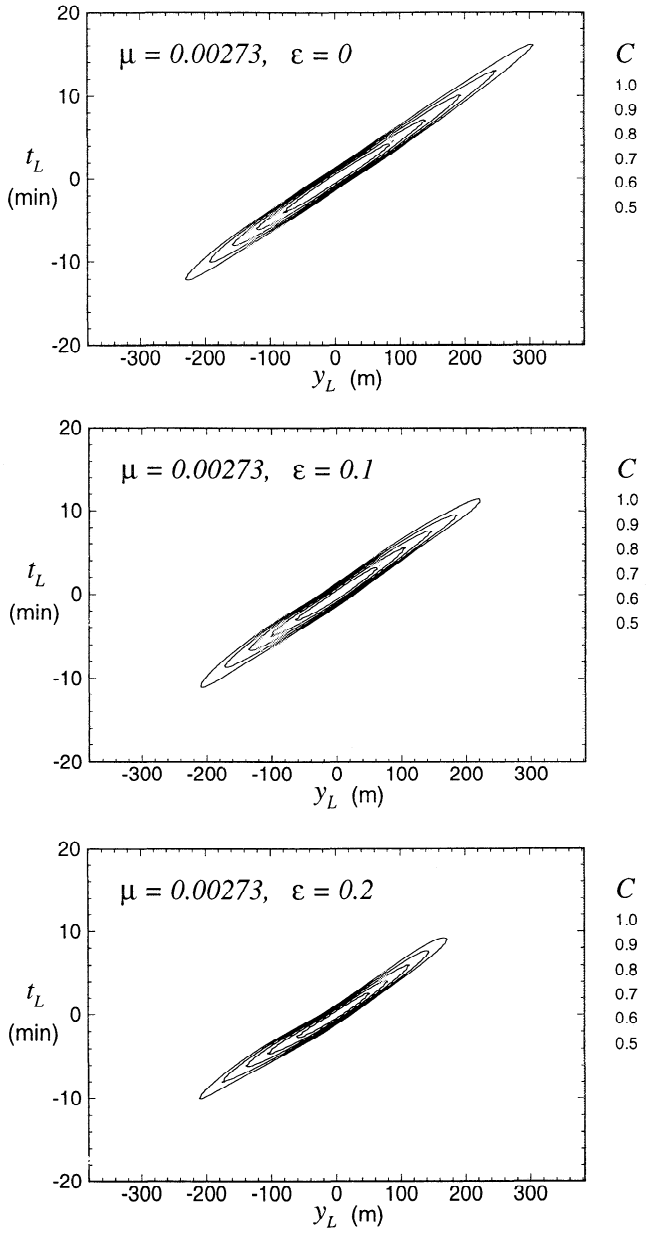

Figure 7. Time- and space-lagged correlations $C(y_L, t_L)$ for the across-shore velocity component $u(x_0, y, t)$ from experiments with $\mu = 0.00273$ m s^{-1}, $\lambda = 273$ m, and different values of ϵ.

The time- and alongshore-averaged across-shore momentum flux $\langle \overline{hu^2} \rangle$ is plotted as a function of x in Figure 9. The experiments at $\mu = 0.00136$ m s^{-1} are plotted with solid lines of different thicknesses and show little variation with ϵ. The four experiments at $\epsilon = 0$ are plotted with the thickest line type (with different dash patterns) and indicate that the across-shore flux of the across-shore momentum increases as μ decreases, with local maxima just outside of the sandbar crest for the three lower frictional experiments. For $\mu > 0.00136$ m s^{-1} the experiments at $\epsilon = 0.2$ (the thinnest line types) generally show greater momentum fluxes near the location of the bar than the corresponding experiments at $\epsilon = 0$.

The spatial distribution of the time-averaged across-shore momentum flux contributions from the perturbations $h\langle u'^2 \rangle$ and mean across-shore velocity $h\langle u \rangle^2$ are plotted in Plate 7 for $\epsilon = 0.2$ and $\mu = 0.00409$, 0.00273, and 0.00136 m s^{-1}. The time averages are for 8 hours. Plates 7a and 7b illustrate that there is significant alongshore nonuniformity in the fields. The magnitude of the contribution from the mean fields decreases and the contribution from the perturbation fields increases with decreasing friction. The local maxima from the mean fields at approximately $x = 100$ m and $y = 50$, 300, and 550 m indicate regions of offshore flow, while those at $y = 180$, 430, and 680 m correspond to regions of onshore directed mean flow. Because the experiment at $\mu = 0.00409$ m s^{-1} is an equilibrated wave confined to the mean current path, we focus our discussion of eddies on the experiments at lower friction. The experiments at $\mu = 0.00273$ and 0.00136 m s^{-1} are highly nonlinear and unsteady, and the local hot spots of eddy activity or perturbation u' velocity support the conclusion drawn from Plate 6 that preferential locations exist for the eddies to form and break away from the sandbar. For $\mu = 0.00273$ m s^{-1} the $h\langle u'^2 \rangle$ contours suggest that the eddies preferentially break away from the mean current at alongshore positions $y_0 \approx 80$, 340, and 600 m, where the mean current is directed offshore and is approaching its farthest offshore excursion and where the water depth is decreasing (upslope) as the current approaches alongshore crests of the sandbar. Plate 7 supports the conclusion that eddies are most strongly generated after the alongshore crests, remain within the mean current through the alongshore troughs, and break away from the mean current when approaching the alongshore crests.

3.4. Vorticity and Momentum Balances

The major terms from the time-averaged vorticity balance (13) are plotted as a function of (x, y) in Plate 8 for $\epsilon = 0.2$ for $\mu = 0.00546$, 0.00409, 0.00273, and 0.00136 m s^{-1} (Plates 8a–8d, respectively). Note the y domain shown is $0 < y < 512$ m. The nonlinear term is divided into two parts, contributions from the time-averaged flow $\overline{NL}$ (14) and contributions from eddies NL' (15). The forcing is the same at each frictional value, and to a very good approximation the sum of the other three terms add up to the forcing. Biharmonic friction makes a small contribution to the balances for $x < 20$ m and a negligibly small contribution for $x > 20$ m and is not shown here.

For $\mu = 0.00546$ m s^{-1} the forcing is balanced by bottom friction and the contribution from the nonlinear time mean flow. The flow is steady, and eddies make no contribution. For decreasing μ the frictional contribution decreases and follows a straighter alongshore path. For each experiment the frictional contribution varies in the alongshore direction, and to a first approximation, increases over alongshore crests, where the water is shallower and decreases over alongshore troughs. This

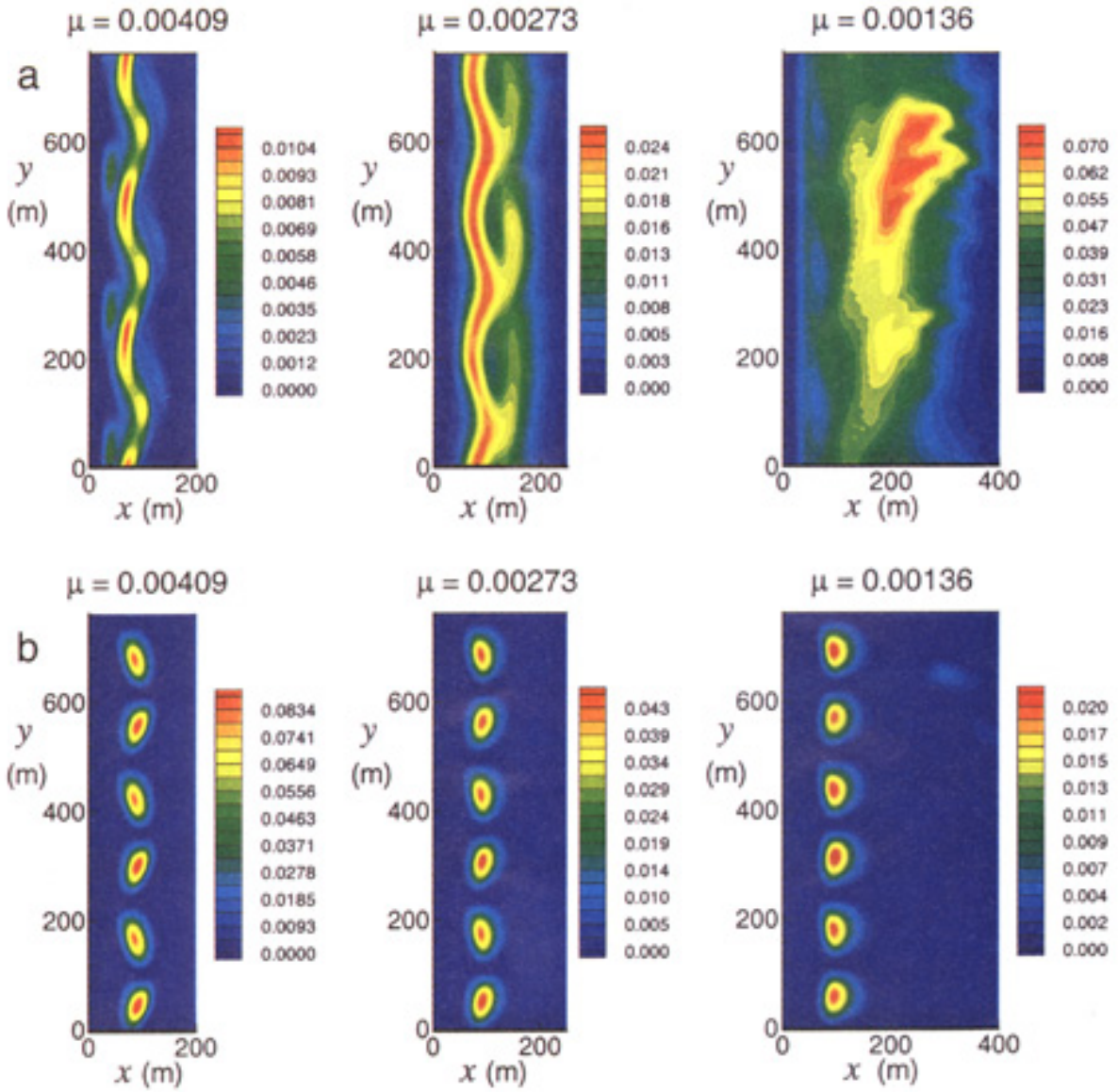

Plate 7. Across-shore fluxes of (a) across-shore momentum by velocity fluctuations $h\langle u'^2\rangle$ $m^3\ s^{-2}$ and (b) of mean across-shore momentum by mean across-shore velocity $h\langle u\rangle^2$ $m^3\ s^{-2}$ for experiments with $\epsilon = 0.2$ and $\mu = 0.00409$, 0.00273, and 0.00136 m s^{-1}.

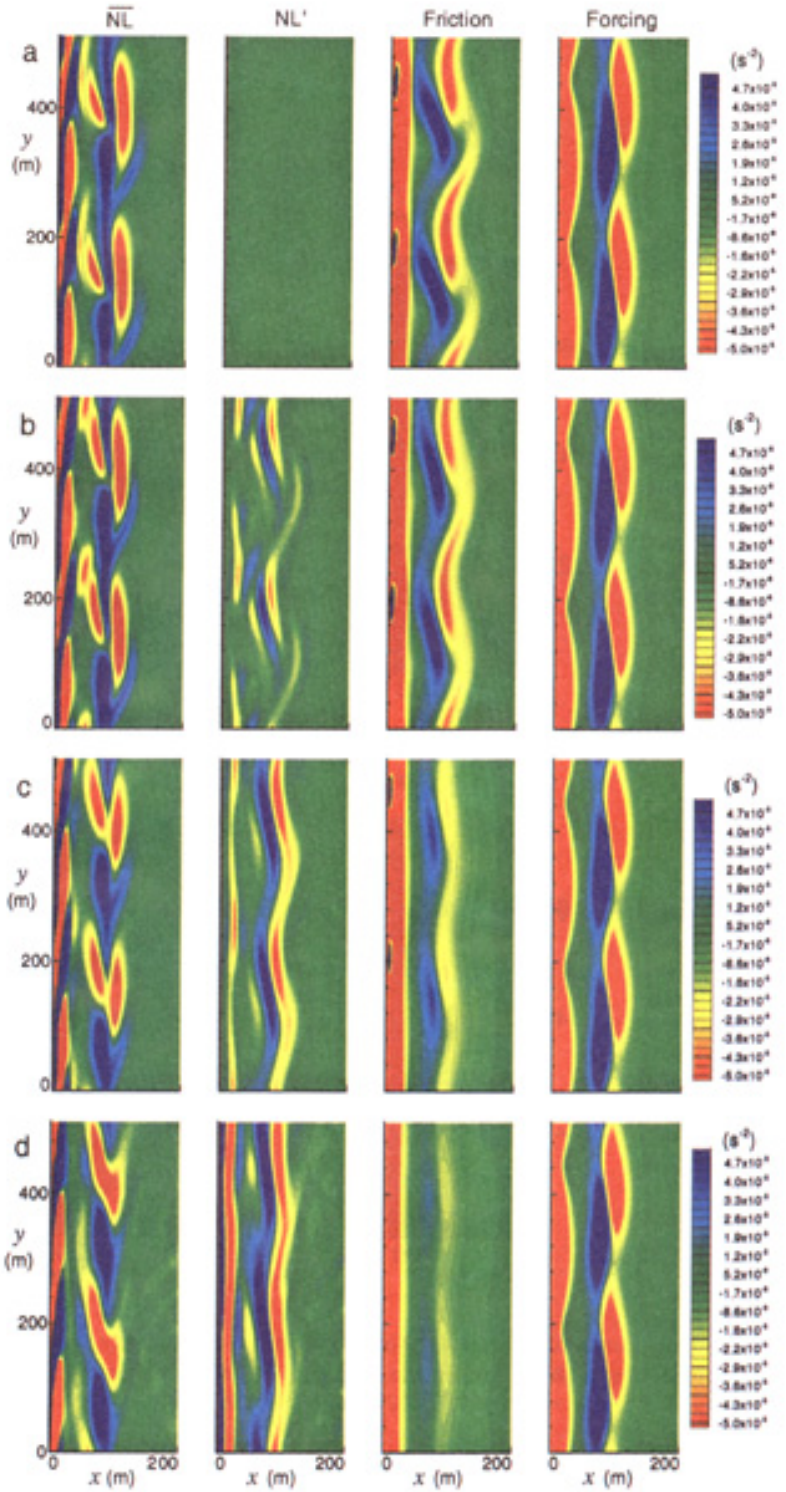

Plate 8. Major terms in the time-averaged vorticity balance equation (13) as a function of (x, y) for experiments with $\epsilon = 0.2$ and $\mu =$ (a) 0.00546, (b) 0.00409, (c) 0.00273, and (d) 0.00136 m s^{-1} (bottom). The time averages are for 8.3 hours from $t = 1.7$ hours to $t = 10$ hours.

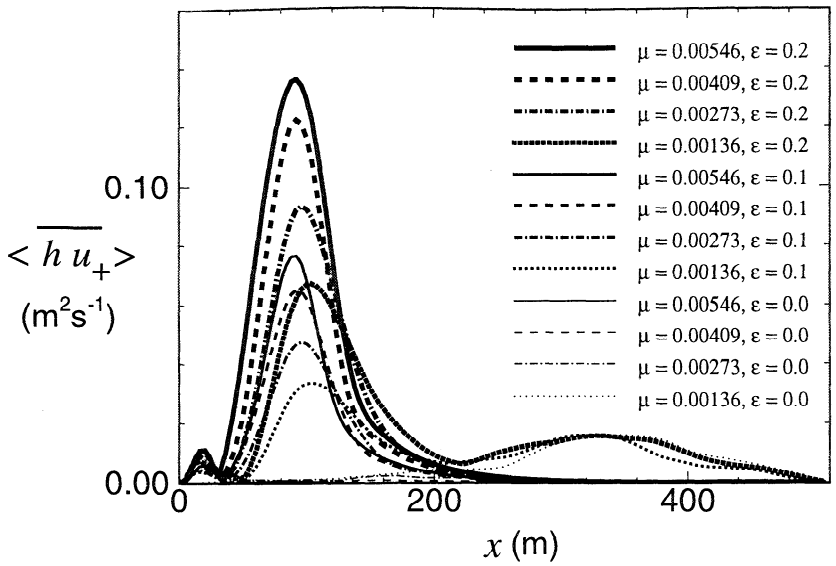

Figure 8. Time- and alongshore-integrated positive across-shore mass flux $\langle \overline{hu_+} \rangle$ for experiments with different values of μ and ϵ for $\lambda = 256$ m.

tendency is more evident for the lower friction experiments where the mean flow is straighter alongshore and does not follow contours of constant depth as closely.

Significantly, as μ decreases, the eddy contribution increases. The eddy term is not uniform in the alongshore direction, indicating that eddies have preferential topographic conditions in which to form, interact, and break away from the mean current. For $\mu = 0.00409$ and 0.00273 m s^{-1}, intensification of the eddy term occurs near $y_0 = 200$ and 450 m at locations of the steepest descending slope. The observation that within the mean current the eddy terms are weakest near $y_0 = 80$ and 300 m suggests that as the current approaches an alongshore crest of the sandbar (upslope), the eddies leave the mean current. This result is consistent with the location of the largest gradients in $\langle \mathrm{KE}' \rangle$ in Plate 6 and also holds for the lowest frictional experiment, though less distinctly because the eddy term is relatively strong along a larger portion of the sandbar. These results are particularly noteworthy because positive contributions

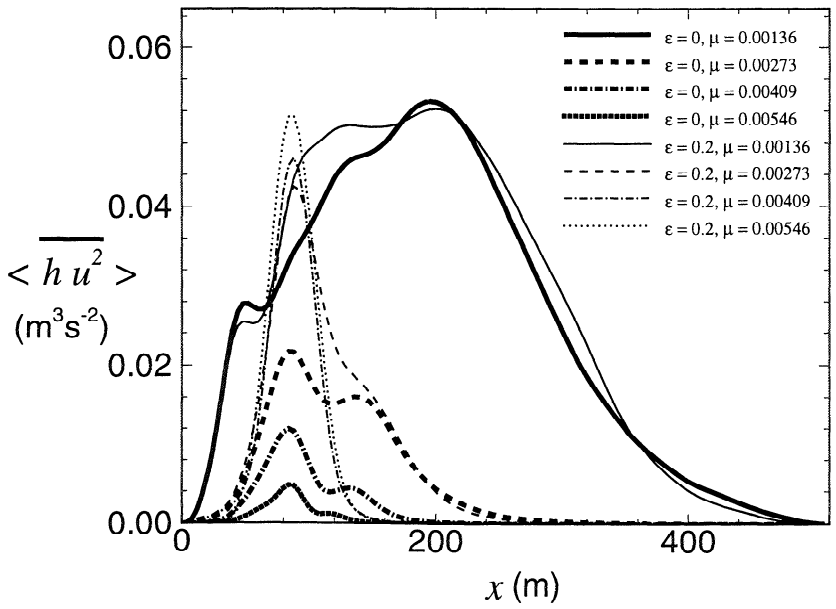

Figure 9. Time- and alongshore-averaged across-shore momentum flux $\langle \overline{hu^2} \rangle$ for experiments with different values of μ and ϵ for $\lambda = 256$ m.

from the eddy term are out of phase with the forcing from the radiation stress and are compensated by the nonlinear mean flow term.

For experiments with $\epsilon = 0$ (not shown), terms of the vorticity balance are approximately alongshore uniform, and the mean nonlinear term is approximately zero, as expected for a long enough time average. Thus, for $\epsilon = 0$ the forcing is balanced by a combination of friction and eddy contributions. As μ decreases, the contribution from friction decreases, and the eddy fields intensify. For $\epsilon = 0.2$ and 0.1 all of the fields in the vorticity balances show strong indications of the topographic length scale and periodicity. This result is expected because the forcing is coupled to the topography through the radiation stress and emphasizes the importance of the radiation stress model.

The terms from the time averaged y momentum balance (11) are plotted for $\epsilon = 0.2$ $\mu = 0.00273$ m s^{-1} at $y_0 = 65$, 129, 193, and 257 m in Figure 10. The dominant contributions come from four terms: forcing $-h\tilde{F}^{(y)}$, bottom friction $\mu\langle v\rangle$, pressure gradient $h\langle p_y\rangle/\rho_0$, and the nonlinear advection term $\langle \mathrm{NL}\rangle = \langle (huv)_x + (hvv)_y\rangle$, which here includes both mean and eddy contributions.

Inside of 20 m, diffusion by the biharmonic friction contributes to the momentum balance as a result of the large gradients in $\langle \overline{v}\rangle$ near the coast. For $x > 20$ m, biharmonic friction plays essentially no role in the momentum balance. The residual term is the sum of the other terms in the equation and is small and would be expected to be zero for a long enough time average over a statistically steady flow. In these experiments, averaged in time over 8 hours, this assumption is approximately satisfied. Positive values for terms in Figure 10 act to decelerate the flow.

The relative strengths and across-shore structure of each term varies with alongshore position. A primary balance at each location is between the forcing and the friction. The across-shore structure of the friction shows the mean velocity profiles $\langle v\rangle$ scaled by μ at different alongshore positions. The forcing is clearly not uniform in y and changes sign in the trough at $y_0 = 193$ m.

The pressure gradients are small at $y_0 = 129$ and 257 m where h achieves minimum (alongshore crest) or maximum (alongshore trough) values. At intermediate depths, where the topography has the steepest slope at $y_0 = 65$ and 193 m, the pressure gradient acts to accelerate or decelerate the flow in the following manner.

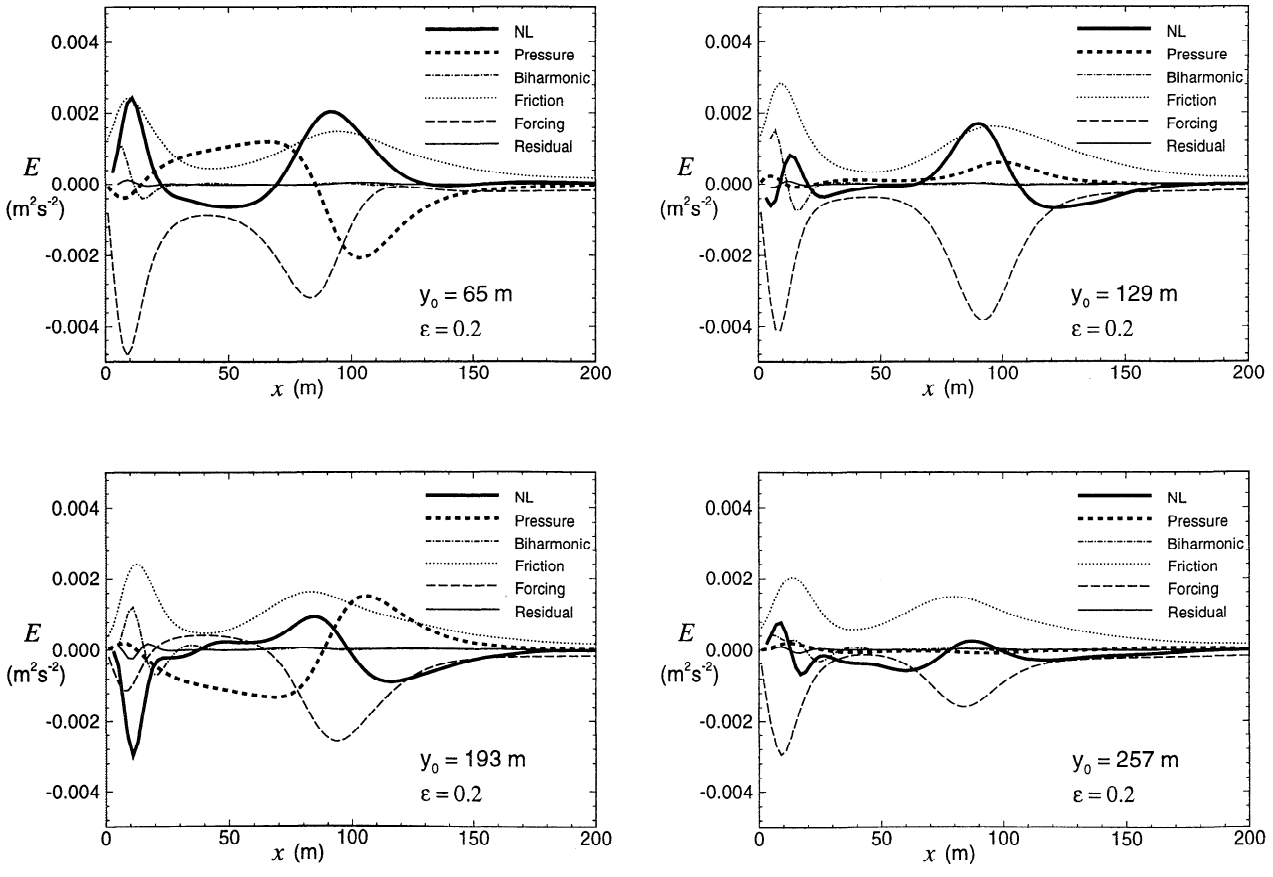

Figure 10. Terms in the time-averaged y momentum equation (11) as a function of x at different y_0 locations for $\mu = 0.00273$ m s^{-1} and $\epsilon = 0.2$.

At $y_0 = 65$ m, over ascending topography, the pressure gradient decelerates the flow in the trough ($20 < x < 80$ m) and accelerates the flow outside of the bar crest $80 < x < 150$ m. At this location the mean current is turning farther offshore, as seen from the streamlines in Plate 6. At $y_0 = 193$ m, over descending topography the pressure gradient acts to accelerate the flow in the trough and over the bar ($20 < x < 90$ m) and decelerates the flow outside of the bar crest $90 < x < 160$ m, where the mean flow is closer to shore.

The effects of the pressure gradient in the trough are compensated by changes in the nonlinear term, which is generally opposed to the pressure gradient, and from local differences in forcing from the gradients of the radiation stresses. In regions where the forcing is stronger than average the pressure gradient adjusts to decelerate the flow and in regions of weaker forcing the pressure gradient compensates to accelerate the alongshore current. The combination of these forces results in velocities in the trough of similar magnitude at different alongshore positions. The nonlinear term represents the time-averaged across-shore flux of alongshore velocity by the mean current and eddies and has the greatest magnitude at $y_0 = 65$ m where the topography has its steepest ascending slope, consistent with the interpretation from Plate 6 that this is the location of the strongest offshore eddy fluxes.

3.5. Hybrid Experiments

Two differences exist between the experiments over uniform alongshore beaches ($\epsilon = 0$) and those over alongshore variable beaches (e.g., $\epsilon = 0.2$). First, the distribution of the forcing through $F^{(x)}$ and $F^{(y)}$ is changed, and second, the dynamic influence of the topography on the steady or time-dependent currents is modified. To isolate and estimate the relative impact of each of these effects, two types of hybrid experiments are examined. In one type of hybrid experiment, forcing determined for the alongshore variable beach ($\epsilon = 0.2$) is applied in numerical experiments over alongshore uniform beaches ($\epsilon = 0$). In the second type of hybrid experiment, uniform alongshore forcing ($\epsilon = 0$) is applied in experiments over alongshore variable beaches ($\epsilon = 0.2$). Results from these two types of hybrid experiments are compared with the standard experiments for $\epsilon = 0.2$.

A prominent characteristic of flows over alongshore variable topography is the across-shore meandering of the time-averaged streamlines. The across-shore extent of the meanders can be quantified by the average rms deviation of the stream function from its alongshore mean M defined in (21). The ratio of M/M_C, where M_C is the value of M for the standard experiments at the same value of μ, is shown for experiments at different values of μ in Table 2.

The largest normalized total across-shore meandering ($\tilde{M}_C = M_C/h_0L_0V_0$) occurs for $\mu = 0.01$ as steady nonlinear effects become significant (see Plate 2). Both effects of topography on time-averaged flows, through variable forcing and interactions with topography, are significant. Hybrid experiments with variable forcing showed a relatively larger proportion of across-shore meandering than did hybrid experiments with variable alongshore topography. The largest differences in relative response occur for higher values of μ with differences decreasing as μ increases.

The separate effects contributing to across-shore meandering do not generally sum linearly to the combined magnitude of M/M_C for the standard experiments. For the steady experiments at $\mu = 0.00546$ m s^{-1}, however, this is nearly the case, with ~55% of the across-shore meandering occurring for variable forcing and 45% occurring for variable topography. For the unsteady flows at $\mu = 0.00273$ m s^{-1}, across-shore meanders in each hybrid experiment are approximately equal, at 55% of M_C.

4. Summary

Results of numerical experiments of the nonlinear development of alongshore currents over sinusoidal barred beaches have been presented. In these experiments the forcing is coupled to the bottom topography through the gradients of the radiation stress that parameter-

Table 2. Parameters From Hybrid Experiments

μ, m s^{-1}	ϵ	Forcing Type	M/M_C	$\tilde{M}_C$	$h_0L_0V_0$, m^3 s^{-1}
0.1	0	variable	0.805		4.23
0.1	0.2	uniform	0.493		4.20
0.1	0.2	standard	1.0	0.0385	4.23
0.01	0	variable	0.623		36.0
0.01	0.2	uniform	0.433		35.5
0.01	0.2	standard	1.0	0.0568	31.2
0.00546	0	variable	0.552		61.1
0.00546	0.2	uniform	0.446		61.4
0.00546	0.2	standard	1.0	0.0381	47.4
0.00409	0	variable	0.599		72.1
0.00409	0.2	uniform	0.509		74.9
0.00409	0.2	standard	1.0	0.0219	67.8
0.00273	0	variable	0.552		86.7
0.00273	0.2	uniform	0.549		86.2
0.00273	0.2	standard	1.0	0.0152	87.2

Normalized average across-shore meanders M/M_C of the time-averaged stream functions, where M is defined in (21) and where M_C is the value of M for experiments with the same value of μ in which the forcing is coupled to the beach topography in the standard manner. The two types of hybrid experiments used are (1) variable forcing, determined with $\epsilon = 0.2$, over alongshore uniform beaches with $\epsilon = 0$ and (2) alongshore uniform forcing, determined for $\epsilon = 0$, over alongshore variable beaches with $\epsilon = 0.2$. Also listed are normalized values for the standard experiments $\tilde{M}_C = M_C/h_0L_0V_0$ and the constants $h_0L_0V_0$, with $h_0 = 1.82$ m and $L_0 = 89$ m.

izes the effects of obliquely incident breaking surface waves and translates that into momentum input. The flow response depends on the dimensionless parameter Q, the topographic perturbation amplitude ϵ, and the wavelength of the topographic variation λ. Different parameter ranges of Q, ϵ, and λ are explored by varying the bottom friction coefficient μ and the beach bathymetry. Numerical experiments have been conducted here across a range of bottom friction coefficients, with both $\mu < \mu_C$ and $\mu > \mu_C$, and significantly different flow regimes are found.

The flows are started from rest. For the alongshore uniform case $\epsilon = 0$, propagating disturbances grow with wavelengths and phase speeds predicted by the linear stability theory. At higher values of μ the effect of variable topography is to stabilize or regularize the flow. The mean alongshore current follows a curvilinear path approximately following contours of constant depth. The wavelength of the mean current is set by the wavelength of the topographic variability λ. Shear waves travel along the curvilinear path and may be equilibrated, fluctuating, or strongly turbulent depending on μ. In each of the different classes of shear flow, shear waves propagate alongshore at a dominant characteristic phase velocity significantly lower than the maximum time mean current velocities.

At lower values of μ the shear waves form patches of vorticity that break offshore from the mean current. For $\epsilon = 0.1$ and 0.2, offshore excursions of eddies preferentially occur at alongshore positions where the mean current is approaching a topographic high in the sandbar and the water is becoming shallower. The region downstream of the sandbar crest, where the water is again becoming deeper, appears to be favorable for the reformation of new eddies from the current instabilities. At the lowest values of friction, inertial effects are stronger, and the flows are strongly turbulent for all values of ϵ examined. For $\epsilon = 0.1$ and 0.2 the time mean current travels a straighter route with a weaker tendency to follow contours of constant depth. Eddies still exhibit a weak preference to break away from the mean current when the mean current is at its farthest offshore excursion, but the eddies also may leave the mean current at any alongshore position depending on turbulent interactions. The eddies may persist offshore of the sandbar for several hours.

Mean and rms velocity and vorticity fields and terms from the momentum and vorticity balances also contain variability at the topographic length scales. In experiments at $\mu = 0.00273$ m s^{-1}, where λ is varied, as λ decreases, the advective timescale $\lambda/\langle v \rangle$ decreases, and the meanders in the mean flow decrease.

Equilibrated waves are distinguishable from the more irregular flows that develop at lower friction by the regularity of the velocity fluctuations in time series and by the strong qualitative differences in appearances of the wavenumber-frequency spectra. For equilibrated shear waves, energy is tightly confined around the particular ω and k values corresponding to the dominant frequency and wavenumber of the steadily propagating waves. For larger topographic variations the energy in equilibrated waves increases at harmonic frequencies and wavenumbers. Wavenumber-frequency spectra show that at low friction ($\mu = 0.00273$ and 0.00136 m s^{-1}) the effect of increasing ϵ is to spread energy to a broader range of wavenumber and frequency generally about a line corresponding to the phase velocity of the unstable vorticity waves $\omega/k = c_0$. For the most turbulent flows, differences with ϵ are less pronounced. There is also substantial energy at zero frequency and at the wavelength associated with the topographic scale.

The time mean alongshore currents $\langle v \rangle$ plotted in Figure 6 demonstrate that at low friction, turbulent eddies caused by shear instabilities of the alongshore current are responsible for diffusing alongshore momentum into the trough. The differences in the strength of currents in the trough are small at different alongshore positions for the low friction experiments. At higher friction the differences between the strength of currents in the trough is predominantly due to the meandering of the mean current and not to the effects of eddies or shear waves. The meandering of the current appears to be strongly associated with differences in the forcing through the gradient of the radiation stresses over variable topography. Where the water is deeper over the sandbar, the surface waves break closer to the shore, and the momentum input through $F^{(y)}$ forces alongshore currents closer to the shore (e.g., Plates 1 and 8). Where the water is shallower over the sandbar, wave breaking and forcing of the alongshore currents occurs farther offshore. These results emphasize the sensitivity of the resulting nearshore circulation to the distribution of the radiation stresses.

A net effect of increasing ϵ is to increase the across-shore fluxes of mass and momentum. This occurs primarily by contributions from the mean current. Contributions to the across-shore fluxes from eddies increase with decreasing μ but are relatively insensitive to changes in ϵ. Another measurable effect of increasing ϵ is the decreasing of the correlation length scales observed by time- and space-lagged correlations.

Alongshore momentum balances at different alongshore positions show that alongshore pressure gradients are associated with acceleration of the flow on the downslope of an alongshore topographic high and with deceleration of the flow on the upslope of the topographic features. Over alongshore crests and troughs the alongshore pressure gradients are negligibly small, and other dynamics, nonlinearity, friction, and forcing, are balanced. Vorticity balances show that the forcing is balanced by friction, eddy fluxes, and mean nonlinear flow. As friction decreases, there is a corresponding increase in the contribution of the eddies. The eddy contribution is not uniform alongshore but is strongest on the downslope phase of the topography.

Hybrid experiments designed to separate the effects of variable forcing from the dynamic influence of the topography on the current show that the relative importance of each mechanism depends on the bottom friction. At higher friction the contribution from alongshore variations in the radiation stress gradients generally produces larger across-shore meanders of the time-averaged alongshore current than are produced by direct topographic interactions. As friction decreases and the flows become increasingly nonlinear, the two complimentary topographic effects become approximately equal in magnitude at producing the across-shore meanderings of the alongshore current, each producing approximately half of the total meandering observed in the coupled experiments. Overall, these experiments have shown that alongshore topographic variability is an important factor in the dynamics of alongshore currents.

Appendix A: Bottom Topography

The depth $h(x,y)$ is given by

$$h(x,y) = \left\{ A_1 \tanh\left(\frac{b_1\, x}{A_1}\right) + \frac{A_1}{\gamma_1}\left[\frac{b_1\, x}{A_1} - \tanh\left(\frac{b_1\, x}{A_1}\right)\right] - A_2 \exp\left[-5\left(\frac{x-x_C}{x_C}\right)^2\right]\right\} \times \left\{1 + \epsilon \exp\left[-5\left(\frac{x-x_C}{x_C}\right)^2\right]\cos\left(\frac{2\pi n y}{L^{(y)}}\right)\right\}, \quad \text{(A1)}$$

where $b_1 = \tan\beta_1 = \tan(0.075)$, β_1 being the linear beach slope close to the shore, $b_2 = \tan\beta_2 = \tan(0.0064)$, β_2 being the beach slope offshore of the sandbar, $\gamma_1 = b_1/b_2$, $x_C = 80$ m is the location of the sandbar, ϵ specifies the magnitude of the alongshore variation, n specifies the number of wavelengths of the sinusoidal topography in the alongshore domain, and coefficients $A_1 = 2.97$ and $A_2 = 1.5$. For $\epsilon = 0$ this beach profile is an approximate fit to topography measured at Duck, North Carolina, on October 11, 1990, as part of the DELILAH field experiment [*Lippmann et al.*, 2000] and was used as beach 2 for the numerical experiments by *Slinn et al.* [1998]. We define $\lambda = L^{(y)}/n$ as the wavelength of the topographic variability and $\lambda^* = \lambda/x_C$ as a nondimensional wavelength.

Appendix B: Solution Procedure for Pressure

The pressure solution method by *Allen et al.* [1996] is modified for variable topography in the following manner. The Poisson equation is derived by multiplying (1b) and (1c) by h and taking the x derivative of (1b) and the y derivative of (1c) and adding and applying (1a) to form

$$(hp_x)_x + (hp_y)_y = \text{RHS}\,, \quad \text{(B1a)}$$

where

$$\text{RHS} = \rho_0\Big\{-(hu^2)_{xx} - 2(huv)_{xy} - (hv^2)_{yy} - \mu(u_x + v_y) + F_x^{(x)} + F_y^{(y)} - \nu\left[(h\nabla^4 u)_x + (h\nabla^4 v)_y\right]\Big\}\,. \quad \text{(B1b)}$$

(For the numerical solutions a comparable equation is derived in finite difference form.) In order to apply the direct pressure solver of *Allen et al.* [1996] to (B1a) and (B1b) we divide $h(x,y)$ into alongshore mean and perturbation parts, $h(x,y) = \overline{h}(x) + \tilde{h}(x,y)$, and solve iteratively for p^{m+1}; namely,

$$(\overline{h}p_x^{m+1})_x + (\overline{h}p_y^{m+1})_y = \text{RHS} - (\tilde{h}p_x^m)_x - (\tilde{h}p_y^m)_y\,. \quad \text{(B2)}$$

The pressure field from the previous time step is used for the first estimate of p^m at a new time level. For $\epsilon = 0.2$ this method converges in approximately four iterations to the tolerance

$$\frac{1}{L^{(x)}L^{(y)}}\sum_0^{L^{(x)}}\sum_0^{L^{(y)}}\left|p^{m+1}(x,y) - p^m(x,y)\right|\Delta x\Delta y < 10^{-10}. \quad \text{(B3)}$$

Appendix C: Radiation Stress Gradients

The forcing terms $F^{(x)}$ and $F^{(y)}$ in (16) and (17) are given by

$$F^{(x)} = -\frac{1}{\rho_0\, h}\left[(S_{xx})_x + (S_{xy})_y\right] \quad \text{(C1)}$$

$$F^{(y)} = -\frac{1}{\rho_0\, h}\left[(S_{yx})_x + (S_{yy})_y\right]\,, \quad \text{(C2)}$$

where ρ_0 is the constant fluid density, $h = h(x,y)$ is the depth, and the components of the radiation stress terms are [*Mei*, 1989]:

$$S_{xx} = \frac{E}{2}\left(\frac{2C_g}{C}\cos^2\theta + \frac{2C_g}{C} - 1\right)\,, \quad \text{(C3)}$$

$$S_{xy} = S_{yx} = E\frac{C_g}{C}\sin\theta\cos\theta\,, \quad \text{(C4)}$$

$$S_{yy} = \frac{E}{2}\left(\frac{2C_g}{C}\sin^2\theta + \frac{2C_g}{C} - 1\right)\,. \quad \text{(C5)}$$

The wave energy and magnitude of the group velocity are defined from

$$E = \rho_0 g H_{\text{rms}}^2/8 \quad \text{(C6)}$$

$$C_g = \frac{\omega}{2\kappa}\left(1 + \frac{2\kappa h}{\sinh 2\kappa h}\right)\,, \quad \text{(C7)}$$

where H_{rms} is the local rms wave height for a narrow-banded wave field, ω is the peak wave frequency, g is the gravitational acceleration (9.8 m s^{-2}), and $\kappa = (k^2 + l^2)^{1/2}$ is magnitude of the wavenumber vector. The magnitude of the wavenumber κ is determined directly from the dispersion relation

$$\omega = \left\{ g \left(k^2 + l^2\right)^{1/2} \tanh\left[\left(k^2 + l^2\right)^{1/2} h\right] \right\}^{1/2} \quad \text{(C8)}$$

for constant ω and specified h by iteration. The mean wave direction angle $\theta = \theta(x, y) = \tan^{-1}(l/k)$. The components of the group velocity are

$$C_g^{(x)} = C_g \cos\theta = C_g \frac{k}{(k^2 + l^2)^{1/2}} , \quad \text{(C9)}$$

$$C_g^{(y)} = C_g \sin\theta = C_g \frac{l}{(k^2 + l^2)^{1/2}} , \quad \text{(C10)}$$

and $C = \omega/\kappa$.

The wave energy equation is used to determine $E(x, y)$:

$$\left(EC_g^{(x)}\right)_x + \left(EC_g^{(y)}\right)_y = -\langle \epsilon_b \rangle , \quad \text{(C11)}$$

where the dissipation function $\langle \epsilon_b(x, y) \rangle$ is determined using [*Thornton and Guza*, 1983]

$$\langle \epsilon_b \rangle = \frac{3\sqrt{\pi}\rho_0 g B^3 f_p}{16} \frac{H_{\text{rms}}^5}{\gamma^2 h^3} \left\{ 1 - \left[1 + \left(\frac{H_{\text{rms}}}{\gamma h} \right)^2 \right]^{-5/2} \right\} , \quad \text{(C12)}$$

where $f_p = 1/T_p$ is the peak frequency of the wave energy spectrum (assumed to be narrow band), γ is a dimensionless breaker index, taken here to be 0.43 (following typical values utilized by *Thornton and Guza* [1986]), and B is an empirical constant that accounts for various breaker intensities. Optimal values of B in the *Thornton and Guza* [1983] model have been reported in the range between $B = 1.5$ [*Thornton and Guza*, 1983] and $B = 0.8$ [*Thornton and Guza*, 1986]. Here we take $B = 1.2$.

We determine the wave angle $\theta(x, y)$ by tracing rays over the variable topography from specified deep water offshore wave angle $\theta_0 = 135^o$ (measured from the offshore direction). Rays are integrated shoreward [*Lighthill*, 1978] using a fourth-order Runge-Kutta technique:

$$\frac{dk}{dt} = -\left.\frac{\partial \omega}{\partial x}\right|_{k,l,y}$$

$$= -\frac{g\left(k^2 + l^2\right)}{2\omega} \operatorname{sech}^2\left[\left(k^2 + l^2\right)^{1/2} h\right] \frac{\partial h}{\partial x} , \quad \text{(C13a)}$$

$$\frac{dl}{dt} = -\left.\frac{\partial \omega}{\partial y}\right|_{k,l,x}$$

$$= -\frac{g\left(k^2 + l^2\right)}{2\omega} \operatorname{sech}^2\left[\left(k^2 + l^2\right)^{1/2} h\right] \frac{\partial h}{\partial y} , \quad \text{(C13b)}$$

$$\frac{dx}{dt} = \left.\frac{\partial \omega}{\partial k}\right|_{l,x,y} = \frac{gk}{2\omega} \left\{ \frac{\tanh\left[\left(k^2 + l^2\right)^{1/2} h\right]}{\left(k^2 + l^2\right)^{1/2}} + h \operatorname{sech}^2\left[\left(k^2 + l^2\right)^{1/2} h\right] \right\} , \quad \text{(C13c)}$$

$$\frac{dy}{dt} = \left.\frac{\partial \omega}{\partial l}\right|_{k,x,y} = \frac{gl}{2\omega} \left\{ \frac{\tanh\left[\left(k^2 + l^2\right)^{1/2} h\right]}{\left(k^2 + l^2\right)^{1/2}} + h \operatorname{sech}^2\left[\left(k^2 + l^2\right)^{1/2} h\right] \right\} , \quad \text{(C13d)}$$

where $h(x, y)$ is given in Appendix A.

The finite difference form of the energy equation (C11) is solved with a fourth-order Runge-Kutta marching procedure in the x direction from an offshore location at $x = x_I$, outside of the region of wave breaking, utilizing second-order centered differences for derivatives in the along-shore y direction. Conditions required at $x = x_I$ include $H_{\text{rms}}(x_I)$, T_P, and $\theta(x_I)$, which are determined from the specified deep water wave angle θ_0 using Snell's law. We take $H_{\text{rms}}(x_I) = 0.7$ m and $T_p = 8$ s at the location $x_I = 512$ m.

The local 1-D model assumes that y derivatives are zero. Thus (C13b) reduces to

$$\frac{dl}{dt} = 0 . \quad \text{(C14)}$$

Given ω and $h(x, y)$, the dispersion relation (C8) is used to calculate $\kappa(x, y)$, which, with $l = \kappa \sin\theta = \text{const}$, gives $\theta(x, y)$. The only terms of the radiation stresses that are retained are $F^{(x)} = -(S_{xx})_x/(\rho_0 h)$ and $F^{(y)} = -(S_{y\dot{x}})_x/(\rho_0 h)$.

Appendix D: Kinetic Energy in Alongshore Modes

The kinetic energy in different alongshore modes is calculated at $x_0 = 100$ m utilizing Fourier transforms of $u(x_0, y, t)$ and $v(x_0, y, t)$ in the alongshore direction. Assuming Fourier component wave solutions for the variables u and v of the form $u(y) = \hat{u}(k)e^{iky}$ and periodicity in y with period $L^{(y)}$, the fields can be expanded in truncated Fourier series with corresponding Fourier coefficients

$$\hat{u}(k_n) = \frac{1}{N} \sum_{j=0}^{N-1} u(y_j) e^{-ik_n y_j} , \quad \text{(D1)}$$

where $y_j = L^{(y)} j/N$, $j = 0, 1, \ldots, N-1$, and k_n are the wave numbers $2\pi n/L^{(y)}$. The mode numbers n range from $n = 0, 1, \ldots, N-1$, where N is the total number of grid points in y [*Canuto et al.*, 1988]. The kinetic energy is defined as a function of the alongshore wavenumbers with

$$\text{KE}(k, t) = \frac{1}{2} \left[\hat{u}(k_n, t)\hat{u}^*(k_n, t) + \hat{v}(k_n, t)\hat{v}^*(k_n, t) \right] , \quad \text{(D2)}$$

where $\hat{u}^*$ is the complex conjugate of $\hat{u}$.

The kinetic energy in different alongshore Fourier mode numbers is plotted on a log scale at early times for experiments at $\epsilon = 0$ and 0.2 for $\mu = 0.00546$, 0.00409, and 0.00273 ms^{-1} in Figure 11. Perturbation energy is forced for mode numbers between 1 and 12. Direct

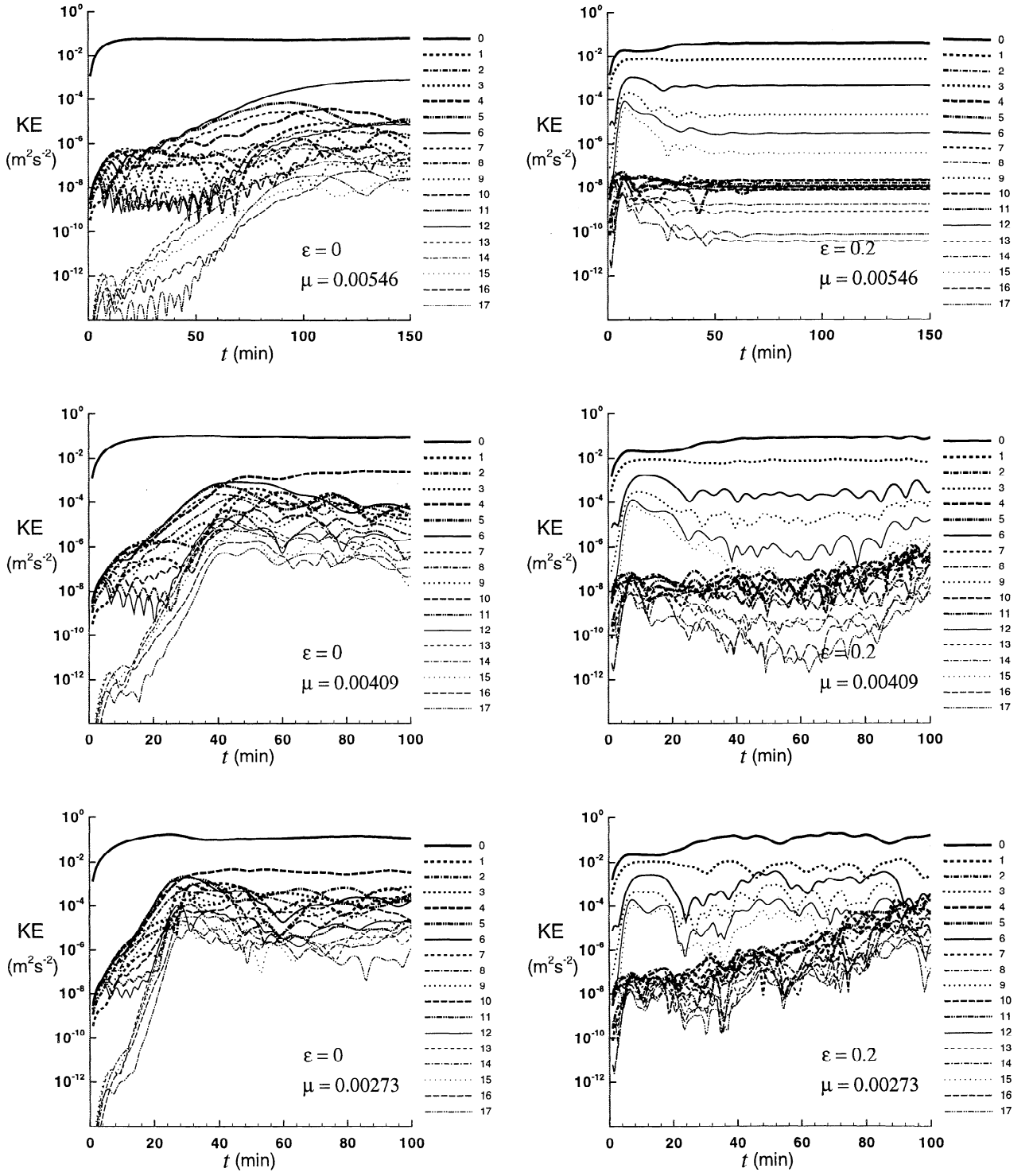

Figure 11. Kinetic energy (D2) in different alongshore wavenumbers corresponding to mode numbers $n = 0 \ldots 17$ as a function of time at $x_0 = 100$ m.

comparison of the observed growth rates for each mode with linear theory is not attempted because the mean currents are steadily increasing during these periods. For experiments at $\epsilon = 0$ the primary forcing occurs at mode 0 (uniform alongshore), and the fastest growing linear mode, mode 6 (128 m), rises out of the noise first in agreement with linear theory. For $\epsilon = 0$ and $\mu = 0.00546$ m s^{-1} an equilibrated shear wave develops at mode 6, which contains approximately an order of magnitude more energy than other modes. For $\epsilon = 0$ and $\mu = 0.00409$ m s^{-1} and $\mu = 0.00273$ m s^{-1}, mode 6 grows fastest for $10 < t < 30$ min, while for $50 < t < 100$ min, mode 4 (192 m) contains the most energy after mode 0.

For $\epsilon = 0.2$ and $\mu = 0.00546$ m s^{-1} each alongshore mode achieves a steady level of energy after approximately $t = 50$ min. The largest energy is in mode 0 (alongshore uniform) followed by modes 3 (256 m), 6 (128 m), 9 (85 m), 12 (64 m), and 15 (51 m). In the experiments with $\epsilon = 0.2$ the primary forcing is at a combination of alongshore modes (e.g., modes 0, 3, 6, 9, 12, and 15) coupled to the alongshore variability of the topography at mode 3 (256 m).

For $\epsilon = 0.2$ and $\mu = 0.00409$ m s^{-1} the dominant alongshore modes (0, 3, 6, 9, and 12) again achieve fairly distinct energy levels that fluctuate in time. The differences between $\mu = 0.00546$ m s^{-1} and $\mu = 0.00409$ m s^{-1} support the observations in Figure 5 of the $\omega - k$ spectra that the energy at later times is mostly at zero frequency for $\mu = 0.00546$ m s^{-1} and at various fixed wavenumbers and frequencies for $\mu = 0.00409$ m s^{-1}.

For $\epsilon = 0.2$ and $\mu = 0.00273$ m s^{-1} the same topographic wavelengths first dominate the flow as for $\mu = 0.00409$ m s^{-1}, but increased nonlinearities cause the primary harmonics (modes 3, 6, 9...) to become obscured by other modes with increasing energy as t increases. At later times the two most energetic modes are from the mean flow (mode 0) and at the topographic wavelength (mode 3) $\lambda = 256$ m.

Acknowledgments. This research was supported by the Office of Naval Research (ONR), Coastal Dynamics Program under grant N00014-95-1-0047. Support was also provided for D.N.S by ONR grants N00014-99-1-0065 and N00014-99-1-0489, for J.S.A. by ONR grant N00014-93-1-1301, and for R.A.H. by ONR grant N00014-96-1-0237. Supercomputer support was provided by the College of Oceanic and Atmospheric Sciences, OSU, through a grant to M. R. Abbott from the NASA Earth Observing System program.

References

Allen, J. S., P. A. Newberger, and R. A. Holman, Nonlinear shear instabilities of alongshore currents on plane beaches, *J. Fluid Mech.*, *310*, 181–213, 1996.

Bowen, A. J., Rip currents, 1, Theoretical investigations, *J. Geophys. Res.*, *74*, 5467–5478, 1969.

Bowen, A. J., and R. A. Holman, Shear instabilities of the mean longshore current, 1, Theory, *J. Geophys. Res.*, *94*, 18,023–18,030, 1989.

Canuto, C., M. Y. Hussaini, A. Quarteroni, and T. A. Zang, *Spectral Methods in Fluid Dynamics,* 557 pp., Springer-Verlag, New York, 1988.

Drazin, P. G., and W. H. Reid, *Hydrodynamic Stability,* Cambridge Univ. Press, New York, 1981.

Durran, D. R., *Numerical Methods for Wave Equations in Geophysical Fluid Dynamics*, 465 pp., Springer-Verlag, New York, 1999.

Keely, J. R., and A. J. Bowen, Longshore variations in longshore currents, *Can. J. Earth Sci.*, *14*, 1897–1905, 1977.

Lighthill, J., *Waves in Fluids,* Cambridge Univ. Press, New York, 1978.

Lippmann, T. C., T. H. C. Herbers, and E. B. Thornton, Gravity and shear wave contributions to nearshore infragravity motions, *J. Phys. Ocean.*, in press, 2000.

Mei, C. C., *The Applied Dynamics of Ocean Surface Waves,* 740 pp., World Scientific Publishing Co., Singapore, 1989.

Oltman-Shay, J., P. A. Howd, and W. A. Birkemeier, Shear instabilities of the mean longshore current, 2. Field data, *J. Geophys. Res.*, *94*, 18,031–18,042, 1989.

Phillips, N. A., An example of non-linear computational instability, in *The Atmosphere and Sea in Motion, Rossby Memorial Volume*, pp. 501–504, Rockefeller Inst. Press, New York, 1959.

Putrevu, U., J. Oltman-Shay, and I. A. Svendsen, Effect of alongshore nonuniformities on longshore current predictions, *J. Geophys. Res.*, *100*, 16,119–16,130, 1995.

Slinn, D. N., J. S. Allen, P. A. Newberger, and R. A. Holman, Nonlinear shear instabilities of alongshore currents over barred beaches, *J. Geophys. Res.*, *103*, 18,357–18,379, 1998.

Thornton, E. B., and R. T. Guza, Transformation of wave height distribution, *J. Geophys. Res.*, *88*, 5925–5938, 1983.

Thornton, E. B., and R. T. Guza, Surf zone longshore currents and random waves: Field data and models, *J. Phys. Oceanogr.*, *16*, 1165–1178, 1986.

Wu, C.-S., E. B. Thornton, and R. T. Guza, Waves and longshore currents: Comparison of a numerical model with field data, *J. Geophys. Res.*, *90*, 4951–4958, 1985.

D. N. Slinn, Department of Ocean Engineering, Florida Atlantic University, 777 Glades Road, Boca Raton, FL 33431-0991 (email: slinn@oe.fau.edu)

J. S. Allen, and R. A. Holman, College of Oceanic and Atmospheric Sciences, Oregon State University, 104 Ocean Admin Bldg., Corvallis, OR 97331-5503. (email: jallen@oce.orst.edu; holman@oce.orst.edu)

(Received August 23, 1998; revised February 25, 2000; accepted February 28, 2000.)